ChemPubSoc Europe

DOI: 10.1002/ejic.201701013

EurJIC European Journal of Inorganic Chemistry

Full Paper

Spin-Crossover Complexes

CLUSTER ISSUE

# Solution and Solid-State Study of the Spin-Crossover $[Fe^{II}(R\text{-bik})_3](BF_4)_2$ Complexes (R = Me, Et, Vinyl)

Siddhartha De,[a] Subrata Tewary,[b] Delphine Garnier,[a,c] Yanling Li,[a] Geoffrey Gontard,[a] Laurent Lisnard,[a] Alexandrine Flambard,[a] Frank Breher,[c] Marie-Laure Boillot,[d] Gopalan Rajaraman,*[b] and Rodrigue Lescouëzec*[a]

**Abstract:** The magnetic properties of three spin-crossover complexes, $[Fe^{II}(R\text{-bik})_3](BF_4)_2 \cdot nH_2O$ (**1**–**3**), based on bis(imidazolyl)ketone ligands, were investigated in solution and the solid state. Their properties were compared with those of the ketone-free analogue, $[Fe^{II}(bim)_3](OTf)_2$ (**4**). The alkyl and vinyl R groups have weak influence on the transition temperature, $T_{1/2}$, in solution, while stronger differences are observed in the solid state, because different intermolecular interactions occur in **1**–**3**. The spin-state equilibria in solution were followed by SQUID magnetometry and the Evans NMR spectroscopy method. Interestingly, the equilibria can also be simply and efficiently probed by following the temperature dependence of an adequately chosen $^1H$ chemical shift. Overall, these experiments give coherent results, with $T_{1/2}$ located between 320 and 335 K, a narrow range, in comparison with the solid state. DFT calculations have allowed the rationalization of the magnetic differences. The molecular-orbital and spin-density calculations reveal that the presence of the C=O group between the imidazolyl units in the ligands of **1**–**3** leads to an extended aromatic system, an effective π-acceptor effect, stabilizing the LS state and reducing the LS–HS gap, in comparison with **4**.

## Introduction

Spin-crossover (SCO) complexes have been the focus of considerable interest for both fundamental and practical reasons. These complexes, whose electronic properties can be reversibly switched by external stimuli (light, temperature, pressure, etc.), are interesting building blocks to design responsive molecular materials. For instance, they appear as good candidates for the development of molecule-based sensors,[1] logic gates[2] and memory[3] and display devices.[4]

The $Fe^{II}$ SCO complexes represent the largest family of SCO complexes, many of them exhibiting an octahedral $\{N_6\}$ coordination polyhedron. In these complexes, the diamagnetic low-spin (LS) configuration ($t_{2g}^6$, $S = 0$) is converted into a paramagnetic high-spin (HS) one ($t_{2g}^4 e_g^2$, $S = 2$). The spin-state switching is associated with significant changes in magnetic or optical properties and the process can thus be followed by magnetometry, optical studies or any other technique. The temperature dependence of the physical values related to the spin state of the molecules allows the determination of the relative amount of the HS and LS fractions. These data can thus be used to extract the thermodynamic parameters associated with the SCO; in particular, the entropic and enthalpic contributions to the spin equilibrium.[5–7] NMR spectroscopy represents another useful tool to follow the spin equilibrium in solution and to determine its associated thermodynamic parameters. The Evans method, which gives indirect access to the magnetic susceptibility of paramagnetic compounds in solution and allows the extraction of the relative amount of the HS fraction, $\gamma_{HS}$, is the most common approach.[6] However, this method often suffers from errors, arising, for example, from the approximations on the paramagnetic solute concentration or from the presence of paramagnetic impurities. As reported by A. Walker et al., the temperature dependence of selected $^1H$ chemical shifts can alternatively be used to investigate spin-crossover equilibria.[7a] This approach has been used in various recent studies of $Fe^{II}$ SCO complexes.[7b–7d] In fact, the NMR spectroscopic chemical shifts are highly sensitive to changes in electronic ground states in transition-metal complexes.[8] Alternatively, magnetic measurements of solutions can be used to follow the temperature dependence of the magnetic susceptibility in a direct manner.[9] However, this method is not so common and it may suffer from approximations; for example, due to an important diamagnetic contribution (arising from the dilution of the paramagnetic species in a diamagnetic solvent). During the last few years, a number of switchable polynuclear complexes featuring derivatives of the bis(1-R-imidazol-2-yl)ketone ligand, R-bik, have been in-

[a] Institut Parisien de Chimie Moléculaire (UMR 8232), Université Paris 06, Sorbonne Universités,
4 Place Jussieu, 75252 Paris CEDEX 5, France
E-mail: rodrigue.lescouezec@upmc.fr
http://ipcm.fr/LESCOUEZEC-Rodrigue
[b] Department of Chemistry, Indian Institute of Technology Bombay, Powai, Mumbai 400076, Maharashtra, India
E-mail: rajaraman@chem.iitb.ac.in
[c] Institut für Anorganische Chemie, Karlsruhe Institut für Technologie (KIT), Campus Süd, Engesserstr. 15, Geb. 30.45, 76131 Karlsruhe, Germany
[d] Institut de Chimie Moléculaire et des Matériaux d'Orsay, Univ. Paris Sud, Université Paris-Saclay, CNRS,
91405 Orsay CEDEX, France

Supporting information and ORCID(s) from the author(s) for this article are available on the WWW under https://doi.org/10.1002/ejic.201701013.

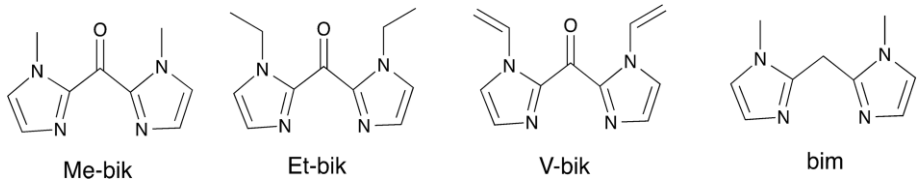


Scheme 1. Bis(imidazolyl) chelate ligands used in this work.

vestigated by some of us (R being a methyl or a vinyl group).[10,11] Cyanide-bridged polynuclear complexes in which the $\{M(R\text{-}bik)_2(NC)_2\}$ subunit exhibits a spin transition (when M = Fe) that can be associated with metal–metal electron transfer (when M = Co) have been reported. In these systems, the switchable properties in the solid state depend not only on the nature of the ligands, but also on various parameters that can be difficult to control (the nature of the crystal phase, the presence of molecules in the crystal lattice, intermolecular interactions).

In the present work, we chose to focus our study on the mononuclear $Fe^{II}$ complexes of the molecular formula $[Fe(R\text{-}bik)_3](BF_4)_2.n(H_2O)$ {Me-bik = bis(1-methylimidazol-2-yl)ketone (**1**), Et-bik = bis(1-ethylimidazol-2-yl)ketone (**2**) and V-bik = bis(1-vinylimidazol-2-yl)ketone (**3**); $n$ = 0.25 (**1**), 0 (**2**) and 1.5 (**3**)} and the paramagnetic derivative $[Fe^{II}(bim)_3](OTf)_2$ (**4**) {bim = bis(1-methylimidazol-2-yl)methane}. The ligands are shown in Scheme 1. The $[Fe(R\text{-}bik)_3]^{2+}$ trischelate complexes are reminiscent of the well-known low-spin $[Fe(phen)_3]^{2+}$ and $[Fe(bipy)_3]^{2+}$ complexes, where 2,2′-bipyridine and 1,10-phenanthroline are the α-diimine ligands.[12,13] However, in the present case, the β-diimine ligands, R-bik, form six-membered rings that induce a weaker ligand field on the $Fe^{II}$ ion, and in some cases, the spin-crossover phenomenon.

Our purpose is to investigate how slight changes in this ligand family can affect the switchable properties of the complexes in solution. More specifically, in this contribution, we have investigated the spin equilibria in solution by using variable-temperature (VT) $^1H$ NMR spectroscopy and have compared the results with the Evans NMR spectroscopic method and solution SQUID magnetometry. We have also compared these results with those obtained in the solid state. In addition, DFT calculations have been performed on the different complexes to probe their electronic structures and rationalize their properties.

## Results and Discussion

### Solid-State Measurements

Complexes **1**–**4** were isolated as dark-blue platelike crystals (**1**–**3**) or colourless needlelike crystals (**4**) from the reaction of $Fe^{II}$ salts with three equivalents of the bis(imidazolyl) chelate ligands.

Cell parameters and space groups are given in Table 1. Their structures (determined at 200 K) consist of trischelate $[Fe^{II}(L)_3]^{2+}$ cationic units (L = R-bik or bim), tetrafluoroborate (**1**–**3**) or triflate (**4**) counteranions and water solvent molecules. In the case of **3**, it was not possible to accurately define the exact position of the crystallization water molecules. As the $BF_4^-$ is disordered over two positions, with a relative occupancy of 1/2, we assume the other position is filled by water. Perspective views of the cationic trischelate complexes are shown in Figure 1 (**3**–**4**) and in Figure S1 (**1**–**2**); selected bond lengths and angles are given in Table 2. In the four complexes, the $Fe^{II}$ ions adopt an octahedral $\{N_6\}$ coordination sphere made of three *N*,*N*-chelate-bonded ligands. The Fe–N bond lengths in **1**–**3** are close to each other and are in the ranges: 1.983(2)–2.008(2) Å (**1**), 1.989(2)–2.005(2) Å (**2**) and 1.977(3)–1.995(3) Å (**3**). In the three complexes, the average Fe–N distance of ca. 1.99 Å is in agreement with the occurrence of an iron(II) low-spin state at 200 K.[14] In contrast, the Fe–N bonds in **4** are significantly longer and range from 2.163(3) to 2.207(3) Å (average: 2.18 Å). These values are coherent with an $Fe^{II}$ high-spin state. Notably, other crystal structures with the $[Fe^{II}(Me\text{-}bik)_3]^{2+}$ cation have already been reported with other counteranions.[15] The crystal structure of $[Fe(Me\text{-}bik)_3](ClO_4)_2$, measured at 298 K, reveals a high-spin $Fe^{II}$ compound with an average Fe–N distance of 2.14 Å, whereas the crystal structures of the complexes $[Fe(Me\text{-}bik)_3]Cl_2$ and $[Fe(Me\text{-}bik)_3](OTf)_2$, determined at 150 K, exhibit an average Fe–N distance of 1.98 Å, which matches well with the distances encountered in **1**–**3**.[14b,14c] The β-diimine ligands form six-membered chelate rings that exhibit average

Table 1. Space groups and cell parameters of **1**–**4** measured at 200 K.

| | **1** | **2** | **3** | **4** |
|---|---|---|---|---|
| Space group | Pbca | *C*2/*c* | $P\bar{1}$ | $P2_1/c$ |
| *a* [Å] | 15.3604(3) | 21.1447(5) | 9.3631(2) | 20.5632(5) |
| *b* [Å] | 11.6415(3) | 16.0717(4) | 11.4700(3) | 11.3824(3) |
| *c* [Å] | 37.4475(7) | 12.7572(3) | 18.6414(4) | 16.2092(4) |
| $\alpha$ [°] | 90 | 90 | 99.121(2) | 90 |
| $\beta$ [°] | 90 | 114.657(1) | 93.443(2) | 90.047(1) |
| $\gamma$ [°] | 90 | 90 | 90.240(1) | 90 |

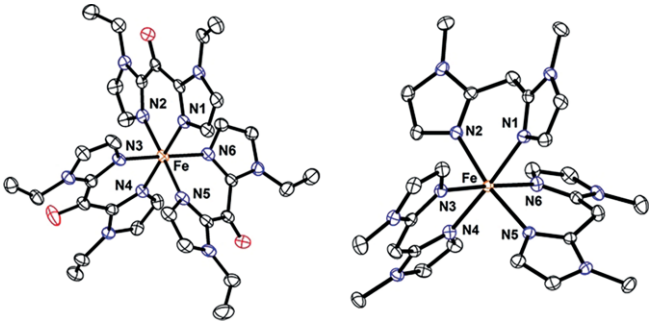


Figure 1. Perspective view (ORTEP) of the: (a) $[Fe^{II}(V\text{-}bik)_3]^{2+}$; and (b) $[Fe^{II}(bim)_3]^{2+}$ cations at 200 K in **3** and **4**, respectively, together with the atomic numbering of their coordination sphere. All hydrogen atoms and counteranions have been omitted for clarity.

Table 2. Structural data related to the geometry of the coordination sphere in **1**–**4**.

| | **1** | **2** | **3** | **4** |
|---|---|---|---|---|
| Temperature [K] | 200(1) | 200(1) | 200(1) | 200(1) |
| $d$[Fe–N(L)]$_{av}$ [Å] | 1.997(11) | 1.997(9) | 1.987(8) | 2.181(19) |
| Bite (N–Fe–N)$_{av}$ angle [°] | 89.1(5) | 89.7(4) | 88.9(9) | 84.2(5) |
| $\sum_{1}^{12}$ \|90 – $\alpha$\| [°] | 13.5(4) | 8.9(3) | 21.2(5) | 42.4(5) |
| *trans*(N–Fe–N)$_{av}$ angle [°] | 178.0(4) | 178.4(6) | 177.6(14) | 174.8(38) |
| Dihedral angles* [°] | 4.03(10), 9.03(9), 11.54(9) | 10.35(8), 10.35(8), 13.02(7) | 2.08(15), 10.77(13), 21.79(15) | 11.87(16), 27.29(14), 34.23(15) |
| Shape factor $S$ (OC-6)[a] | 0.042 | 0.019 | 0.063 | 0.314 |

[a] See text for details.

bite angles of 89.1(5)° (**1**), 89.7(4)° (**2**), 88.9(9)° (**3**) and 84.2(5)° (**4**). The values found in **1**–**3** are closer to orthogonality than those of other LS Fe$^{II}$ complexes made of α-diimine ligands with five-membered chelate rings, such as the well-known LS $[Fe^{II}(phen)_3]^{2+}$ complex (with bite angles of ca. 82.8°).[12b] The sum of the deviation from orthogonality of the twelve *cis*-N–Fe–N angles (denoted as $\Sigma$)[16] is relatively small in **1**–**3** [respectively: 13.5(4)°, 8.9(3)° and 21.2(5)°] and indicates a moderate distortion of the octahedral coordination sphere. In contrast, this value reaches $\Sigma$ = 47.6° within the related LS $[Fe(phen)_3]^{2+}$ complex. The $\Sigma$ values in **1**–**3** are also significantly smaller than the one measured in the HS $[Fe(bim)_3]^{2+}$ [$\Sigma$ = 42.4(5)°]. The continuous-shape-measures analysis (CShM)[17,18] allows a more precise quantification of the deviation of the coordination spheres from an ideal geometry. The distortion of the coordination sphere reflects the spin state of the Fe$^{II}$ ion: in the present case, very small values of the shape factor[16,17] are observed in **1**–**3** (Table 2), indicating an almost perfect octahedral surrounding, whereas a higher one is obtained in **4**, as expected for a HS Fe$^{II}$ complex.

The bim and R-bik β-diimine ligands exhibit dihedral angles between imidazole rings, which can vary significantly from one ligand to another within the same complex: 4.03(10)°, 9.03(9)° and 11.54(9)° (**1**); 10.35(8)°, 10.35(8)° and 13.02(7)° (**2**); 2.08(15), 10.77(13)° and 21.79(15)° (**3**); and 11.87(16)°, 27.29(14)° and 34.23(15)° (**4**). The three complexes **1**–**3** exhibit the same average C=O bond length, which amounts to 1.22(1) Å; however, significant differences in the Fe–C–O angles are observed for the three compounds. While the Fe–C–O angle approaches linearity for **1** [ranging from 173.2(2)° to 178.1(3)°] and **2** [from 177.0(2)° to 180°], they deviate significantly from 180° in **3** [from 160.5(3)° to 169.8(4)°]. Overall, these data show that these β-diimine ligands are more flexible than the α-diimine ligands, such as the 1,10-phenanthroline.

Finally, there are no important intermolecular interactions in **1**–**4**, neither strong hydrogen bonding nor π–π interactions. However, short contacts (with interatomic distances shorter than the sum of the van der Waals radii) are found between the C–H groups from the methyl and ethyl substituents and the perpendicularly oriented imidazole ring planes. Thus, the crystal packing of these complexes is most probably influenced by these CH···π interactions between the imidazolyl ring and the alkyl proton. Such a CH···π interaction is often referred to as a point-to-face or T-shaped arrangement,[19] and their energies lie in the range of 1–2 kJ mol$^{-1}$.[20] In **1** and **2**, the average distance of the CH···C(π) contacts are 2.78 and 2.77 Å, respectively. These distances are quite significant, as they lie at the middle of the accepted distance range for such supramolecular interactions (from 2.6 to 3.1 Å).[21] The amplitude of these interactions is also described by the intermolecular CH···ring–centroid distance, which amounts to 2.65 Å in **1** and 2.67 Å in **2** for the shortest contact. The interaction is much more important in **2**, although both values remain within the accepted range.[20] The CH···C(π)/CH···ring–centroid interactions are also more prominent in **2**, as they involve pairs of interactions running along the *z* axis: two of the Et-Im groups of the same Et-bik ligand act simultaneously as donors and acceptors (Figure 2). In compounds **3** and **4**, no significant intermolecular CH···C(π)/CH···ring–centroid short interactions (less than sum of the C–H van der Waals radii) are found.

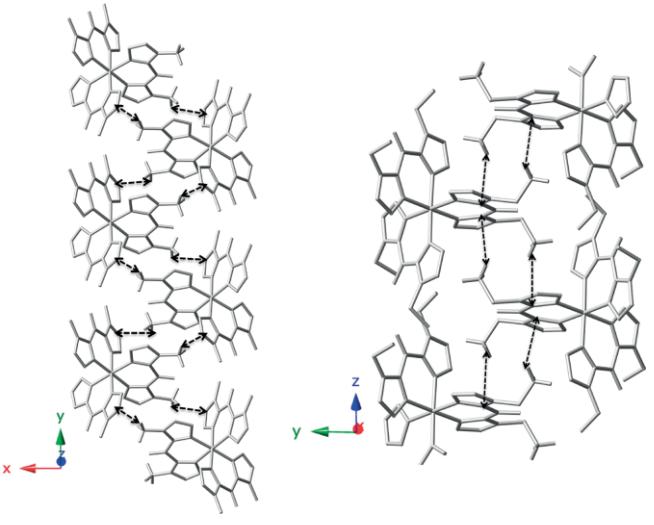


Figure 2. View of the intermolecular C–H···π interactions (black dotted lines) between adjacent complexes in **1** (left) and **2** (right). H atoms not involved in interactions have been omitted for clarity.

## Magnetic Properties in the Solid State

The $\chi_M \times T$ versus $T$ curves for **1**–**4** (measured on fresh microcrystalline powders introduced into the magnetometer at low temperature to avoid solvent loss) are depicted in Figure 3 ($\chi_M$ being the molar magnetic susceptibility per Fe$^{II}$ complex).

The $\chi_M \times T$ product of **4** is almost constant between 50 and 400 K and the measured value, 3.55 cm$^3$ mol$^{-1}$ K, is coherent with that expected for a high-spin Fe$^{II}$ complex ($S$ = 2, $g \approx$ 2.18). In contrast, the $\chi_M \times T$ curves of **1**–**3** exhibit sigmoidal shapes

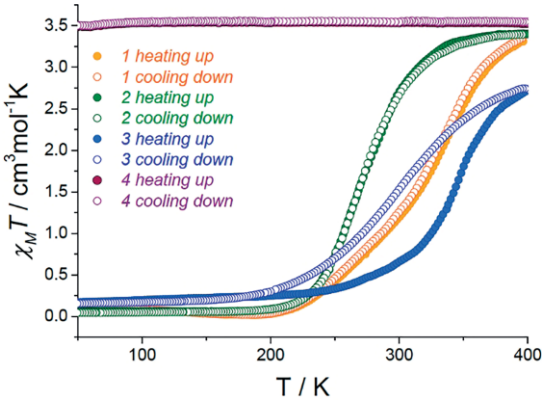


Figure 3. Solid-state study of the spin-crossover $[Fe^{II}(R\text{-bik})_3](BF_4)_2$ complexes [R = Me, Et, vinyl].

that are typical of spin-crossover complexes. While weak $\chi_M \times T$ products measured at low temperature (ca. 0.15, 0.06 and 0.01 $cm^3\ mol^{-1}\ K$ for fresh samples of **1**, **2** and **3**, respectively) are in agreement with an $Fe^{II}$ low-spin ion ($S = 0$), upon warming from 180 to 400 K, the $\chi_M \times T$ values gradually increase, reaching ca. 3.11 (**1**), 3.40 (**2**) and 2.80 (**3**) $cm^3\ mol^{-1}\ K$ at 400 K. These values are lower than those expected for $Fe^{II}$ high-spin ions (with $\chi_M \times T \approx 3.55\ cm^3\ mol^{-1}\ K$ and $g \approx 2.17$) and they are inferior to the measured value in the analogue compound **4**. They point to incomplete spin crossover. The spin crossover observed upon cooling (and over several cycles) is identical for **1** and **2**. In contrast, for compound **3**, the $\chi_M \times T$ product reverts to the diamagnetic state by following a different path upon cooling. This is associated with the loss of crystallization water molecules at high temperature, as confirmed by thermogravimetric analysis (see the Supporting Information). Indeed, a previously dehydrated sample, **3d**, exhibits the same $\chi_M \times T$ curve as that observed in the cooling mode after heating in the SQUID to 400 K. Once dehydrated, the spin transition of **3d** is reversible upon cycling. The transition temperatures, $T_{1/2}$, of the spin transitions for these compounds are ca. 316 (**1**), 277 (**2**), 342 (**3**, fresh) and 302 K (**3d**, dehydrated). The shift of 40 K observed between **3** and **3d** reveals the impact of the presence of solvate molecules in the crystal lattice on the SCO phenomenon in the solid state.[22]

The solid-state $\chi_M \times T$ versus $T$ data of **1**–**3** were fitted as commonly described in the literature by using the Slichter-Drickamer mean-field model [Equation (1)][23] to calculate the spin-equilibrium curves, with an estimate of the associated thermodynamic parameters.

$$\ln\left[(1-n_{HS})/(n_{HS}-f_{Hs})\right] = \left[\Delta H + \Gamma(f_{HS}+1-2n_{HS})\right]/RT - \Delta S/R \quad (1)$$

$\Delta H$ and $\Delta S$ are the enthalpy and the entropy variations at the experimental transition temperature ($T_{1/2}$), whereas the $\Gamma$ parameter accounts for the cooperativity associated with the spin crossover ($f_{HS}$ is the residual HS molar fraction at low temperature and $n_{HS}$ represents the HS molar fraction).

Good fits were obtained for compound **2** (upon heating and upon cooling, respectively) and for the dehydrated sample of **3d**, leading to the following values: $\Delta H$ = 29.3 and 29.6 kJ $mol^{-1}$ (**2**), 32.9 kJ $mol^{-1}$ (**3d**); $\Gamma$ = 0.78 and 0.45 kJ $mol^{-1}$ (**2**), 1.0 kJ $mol^{-1}$ (**3d**); $\Delta S = \Delta H/T_{1/2}$ = 107.2 and 107.4 J $K^{-1}$ $mol^{-1}$ (**2**), 100.0 J $K^{-1}$ $mol^{-1}$ (**3d**) (see the Supporting Information). The model partly fails in reproducing the experimental curve of **1** and **3** (fresh sample). This is not unusual for SCO systems; the search for more sophisticated models has been discussed earlier.[24,25] In the cases of **1** and **3**, the loss of solvent molecules during the experiment alters the shape of the spin transition and makes the simulation of the curves not so relevant (the transition temperatures are above room temperature and the experiments are carried out under reduced helium pressure). Overall, the $\Gamma$ values are moderate and the $\Gamma/2RT_{1/2}$ ratios are well below unity, as expected for gradual conversions. This is consistent with the weak intermolecular interactions that are observed in the crystal lattices of **1**–**3**. The estimated enthalpy ($\Delta H$) and entropy ($\Delta S$) values for **2**–**3d** are slightly above the usual range of the typical values observed for SCO compounds ($\Delta H$ = 3–27 kJ $mol^{-1}$ and $\Delta S$ = 22–94 J K $mol^{-1}$).[26,27] However, such high values of enthalpy and entropy variations have been already found in some cases of $Fe^{II}$ SCO complexes.[7b,28] Here, the $\Delta S$ value is particularly high, well above the expected value, due to the electronic entropy change [$\Delta S_{elec} = R \times (\ln 5) = 13.4$ J $K^{-1}$]. This points to the occurrence of important vibrational contributions, $\Delta S_{vib}$. The $\Delta S_{vib}$ partly arises from the variation in the metal–ligand bond strengths that accompany the changes in the metal–ligand bond lengths upon the spin-state change. In the present case, a noticeable contribution to $\Delta S_{vib}$ can also come from conformational changes occurring in the coordinated R-bik ligands (e.g., changes in the Fe–C–O angle and the planarity of the imidazolyl groups). As mentioned above, the β-diimine R-bik ligands are flexible, in contrast with α-diimine ligands, such as 2,2′-bipyridine or 1,10-phenanthroline. Interestingly, we have recently shown that the planarity of the R-bik ligand can be notably affected in Fe–Co charge-transfer systems by the electronic-state of the coordinated metal.[29] Upon conversion of the high-spin $Co^{II}$ into a low-spin $Co^{III}$, the ligand changes from a planar geometry (where the imidazolyl rings are located in the same plane) to a bent one, where the π-delocalization is lost. Such geometrical modifications alter not only the M–L vibrational modes, but also those of the ligands. The bending of the ligand will also affect its π-acceptor ability and contribute to significant change in the M–L bond strength and the enthalpy variation between the two spin states. Unfortunately, here, the loss of crystallinity of **1**–**3** at room temperature did not allow us to obtain the crystal structure of the high-spin state.

The light-induced excited spin-state trapping (LIESST) effect was investigated for the SCO complexes **1**–**3** (both fresh and dehydrated) by irradiating the samples at 20 K with laser diodes at 808, 635, 532 and 405 nm (ca. 5–10 mW $cm^{-2}$). Compounds **2** and **3d** do not show any photomagnetic effect in the present experimental conditions, whereas compounds **1** (Figure 4) and **3** (see the Supporting Information) exhibit, respectively, a moderate and a noticeable increase of their magnetization upon irradiation. The irradiation at 635 nm appears to be the most efficient in both cases. This wavelength is located near the maximum of an intense absorption band, which is observed in the

solid-state UV/Vis measurements (see the Supporting Information). This band is ascribed to a metal-to-ligand charge transfer (MLCT) band, as confirmed by theoretical calculations (see the Supporting Information). The irradiations at 532 nm (near the broad maximum of the MLCT band), at 808 nm (located in the tail of the MLCT band) and at 405 nm (located in a band ascribed to an intraligand transition) also show some efficiency. The $\chi_M \times T$ values reached after 50 min (of irradiation at 635 nm), 0.45 $cm^3\ mol^{-1}\ K$ (**3**) and 2.39 $cm^3\ mol^{-1}\ K$ (**1**), are lower than expected for a HS $Fe^{II}$ complex and they suggest a partial conversion of the diamagnetic state into a photoinduced paramagnetic state. The metastable states relax upon heating the samples (0.3 $K\ min^{-1}$) at $T_{LIESST}$ = 57 K (**3**) and 50 K (**1**).

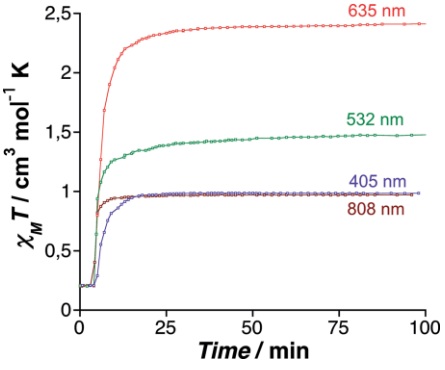


Figure 4. $\chi_M \times T$ versus irradiation time for **1** at 20 K under irradiation at 405, 532, 635 and 808 nm (ca. 5–10 mW $cm^{-2}$).

## Solution Studies

Magnetic susceptibility versus temperature measurements on solids are often used to determine the relative amounts of HS and LS species. Their application to solutions, although possible, imply some experimental complications. As the spin equilibrium is often accompanied by changes in the optical properties, spin equilibrium can also be studied by measuring the temperature dependence of an absorption band, which is characteristic of one of the two spin states. For example, in $Fe^{II}$ complexes bearing π-acceptor ligands, the intensity of the MLCT band can be monitored to follow a spin-state change. However, these experiments often require low-concentration solutions (ca. $10^{-4}$ M), which can lead to the dissociation of the complexes and erroneous data. To avoid this problem, it is better to use techniques that allow one to work at higher concentrations. In the following section, we compare different techniques, including variable-temperature (VT) $^1H$ NMR spectroscopy, the Evans NMR spectroscopic method and solution-state SQUID magnetometry, for the investigation of the spin equilibria of **1**–**3** in acetonitrile solution.

### $^1H$ NMR Spectroscopic Solution Study

#### *Basic Concepts of Paramagnetic NMR Spectroscopy*

The basic concepts of paramagnetic NMR spectroscopy were established several decades ago.[7,8] The main differences between the NMR spectroscopy of diamagnetic and paramagnetic species arise from the occurrence of a hyperfine interaction between the observed NMR nuclei and the unpaired electron(s). This interaction has two major impacts on the NMR spectrum: (1) it leads to strongly shifted signals, which can appear far outside of the normal range of diamagnetic molecules, making the structural analysis more difficult than for a diamagnetic sample;[30] and (2) the NMR spectroscopic signals can be significantly broadened (or even undetectable in some cases), due to fast nuclear relaxation. As the nuclear relaxation is inversely related to the electronic one,[31] the shorter the electronic relaxation times of the metal complex, the sharper the NMR spectroscopic signals. In some favourable cases, such as for $Co^{II}$ octahedral paramagnetic complexes, spectra with good resolution can be obtained,[32,33] so that it is possible to follow – as for diamagnetic species – chemical equilibria by using VT NMR spectroscopic studies (e.g., substitution and isomerization processes).[32] Although the situation of HS $Fe^{II}$ complexes is less favourable, some of these complexes can lead to well-resolved NMR spectroscopic features.[32,33] This is the case in our present study (see below).

In paramagnetic species, the chemical shifts bear structural information, but also some magnetic information. Indeed, the observed chemical shift, $\delta_{obs}{}^T$, can be expressed as the sum of a paramagnetic and a diamagnetic contribution:

$$\delta^T_{obs} = \delta_{dia} + \delta^T_{para} \quad (2)$$

The diamagnetic chemical shift contains the usual contributions to the chemical shift, which exist in diamagnetic molecules. It is generally estimated by measuring an isostructural diamagnetic reference. The paramagnetic chemical shift, $\delta_{para}{}^T$, arises from the hyperfine interaction. $\delta_{para}{}^T$, which depends on the temperature, $T$, can be further decomposed as the sum of the pseudocontact term ($\delta_{PC}$) and the Fermi-contact term ($\delta_{FC}$):

$$\delta^T_{para} = \delta^T_{PC} + \delta^T_{FC} \quad (3)$$

The Fermi-contact term is a through-bond electron–nuclear interaction. It arises from the electron-spin delocalization onto the observed nucleus (in other words, the spin density on the nucleus). As mentioned by McGarvey, the Fermi-contact term can be expressed as a function of the magnetic susceptibility:[34]

$$\delta^T_{FC} = \frac{A^H}{3(\gamma_N/2\pi)\beta}\left(\frac{\chi_x}{g_x} + \frac{\chi_y}{g_y} + \frac{\chi_z}{g_z}\right) \quad (4a)$$

where $A^H$ is the hyperfine coupling constant, $\gamma_N$ is the gyromagnetic ratio and $\chi_i$ and $g_i$ are the components along the magnetic tensor axes. For a spin-only (S) isotropic system with no populated excited state, the formula is often simplified to:

$$\delta^T_{FC} = \frac{A^H g_{av}\beta}{3\gamma_N kT} S(S+1) \quad (4b)$$

where $g_{av}$ is the average $g$ value and $k$ is the Boltzmann constant. The contact chemical shift can thus be seen as a local paramagnetic susceptibility and its temperature dependence is proportional to $1/T$, in agreement with the Curie law.

The pseudocontact term, $\delta_{PC}{}^T$, is a through-space electron–nuclear interaction and it comes from the dipolar coupling be-

tween the nuclear magnetic moment and the magnetic moment of the unpaired electron. This term strongly depends on the local magnetic anisotropy. For the simple case of an axial *g* tensor, it can be expressed through the simplified following equation:[8,34]

$$\delta_{PC} = \frac{\mu_0}{4\pi}\frac{\beta S(S+1)}{9kT}\frac{3\cos^2\theta - 1}{r^3}(g_{//}^2 - g_{\perp}^2) \quad (5)$$

where $\beta$ is the Bohr magneton, $g_i$ are the components along the magnetic tensor axes, *r* is the distance between the magnetic source and the probed nucleus and $\theta$ is the angle between the main magnetic axis and the *r* direction. This term is small if the local magnetic anisotropy remains moderate. It also strongly depends on the geometrical parameters. It can be negligible if the distance *r* is large, if the angle $\theta$ is close to 54° ($3\cos^2\theta - 1 \approx 0$).[35] However, in some cases, when the anisotropy is not negligible and the geometric parameters make the dipolar contribution not negligible, a deviation from the Curie law is observed. In these cases, the temperature dependence of the chemical shift can only be simulated by including additional terms (generally proportional to $1/T^2$).

In summary, if the dipolar contribution remains moderate for a given proton, the temperature dependence of the chemical shift will strictly follow a Curie behaviour. It is thus possible to follow spin-crossover equilibria by studying the temperature dependence of selected chemical shifts.[6,36] In fact, as the $Fe^{II}$ spin-state switching is faster than the NMR timescale, the observed proton NMR spectroscopic resonances represent the population-weighted average of the HS and LS states of the molecule at a given temperature. The peak shift is thus related to the amount of high-spin species:

$$\%_{HS} = \frac{(\delta_{obs}^T - \delta_{LS})}{(\delta_{HS} - \delta_{LS})} \times 100 \quad (6)$$

Here the $\delta_{LS}$ is the chemical shift observed for the pure diamagnetic $Fe^{II}$ LS complex ($S = 0$) and it thus represent the $\delta_{dia}$ contribution. The accurate determination of the $\delta$ values for purely HS or LS species is not always accessible because of the limited temperature range (due to experimental limitations). In such cases, the $\delta_{HS}$ or $\delta_{LS}$ values can still be estimated by using the Boltzmann law.

### *NMR Spectra of 1-3*

The NMR spectra of **1**–**3** (in $CD_3CN$ at 310 K), together with the peak assignments, are shown in Figure 5. The values are summarized in Table 3, together with the values for the bis(imidazolyl) chelate ligands. These spectra are typical of paramagnetic species and contain (moderately) broad and strongly shifted temperature dependent signals.[37] In addition to the expected protons from the complexes (with up to five proton environments), each spectrum exhibits residual $CHD_2CN$, water and THF signals. In the case of **2**, small but noticeable signals, due to the presence of free ligands, are always observed. The signal assignment of the $[Fe^{II}(R\text{-bik})_3](BF_4)_2$ complexes was done by using: (i) the relative integration of the signals; (ii) the comparison of the three derivatives (chemical substitution); and (iii) the broadening of the signal. Indeed, the major contribution to the nuclear relaxation arises from the dipolar contribution, which is proportional to $1/r^6$ (where *r* is the distance between the metal centre and the NMR nucleus).[8a] The protons close to the paramagnetic source can thus be identified, as they show a broader signal half-width.

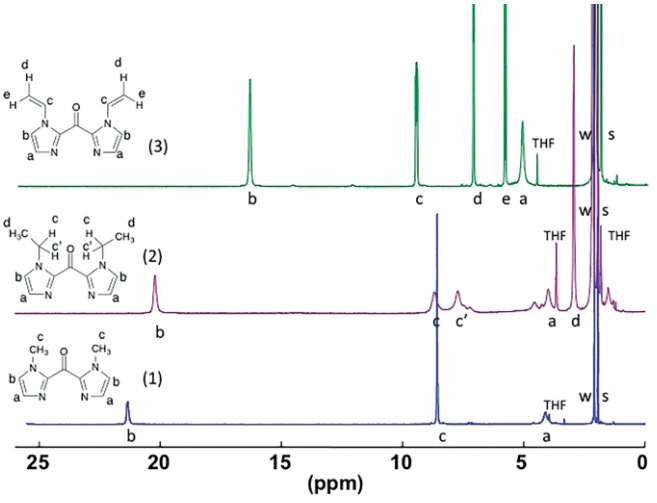


Figure 5. $^1H$ NMR spectra of the complexes $[Fe(Me\text{-bik})_3](BF_4)_2$ **(1)**, $[Fe(Et\text{-bik})_3](BF_4)_2$ **(2)** and $[Fe(V\text{-bik})_3](BF_4)_2$ **(3)** in $CD_3CN$ at 310 K (w: water; s: solvent).

Table 3. Proton NMR spectroscopic data ($\delta$ [ppm]) at 310 K in $CD_3CN$.

| | $H^a$ | $H^b$ | $H^c$ | $H^{c'}$ | $H^d$ | $H^e$ |
|---|---|---|---|---|---|---|
| Me-bik | 7.12 | 7.24 | 3.92 | | | |
| Et-bik | 7.40 | 7.04 | 4.51 | | 1.45 | |
| V-bik | 7.22 | 7.68 | 5.07 | | 7.57 | 5.51 |
| $[Fe(Me\text{-bik})_3](BF_4)_2$ (**1**) | 4.10 | 21.34 | 8.57 | | | |
| $[Fe(Et\text{-bik})_3](BF_4)_2$ (**2**) | 3.99 | 20.22 | 8.69 | 7.73 | 2.93 | |
| $[Fe(V\text{-bik})_3](BF_4)_2$ (**3**) | 5.17 | 16.46 | 9.55 | | 7.20 | 5.89 |

In the spectrum of **1**, the three signals of the Me-imidazole groups are observed with relative intensities of 1:1:3. At 310 K, the sharp signal at $\delta$ = 8.57 ppm (c), with a relative intensity of 3 H, is unambiguously attributed to the $CH_3$ group of the ligand. The two signals with relative intensities of 1 H come from $H^a$ and $H^b$. The broad signal near 4.10 ppm is assigned to $H^a$, which is closer to the paramagnetic $Fe^{II}$ centre. The other signal at $\delta$ = 21.34 ppm is then attributed to the proton $H^b$.

In the spectrum of **2**, four different signals are observed for the Et-imidazole groups, with relative intensities of 1:1:2:3. The sharp signal at $\delta$ = 2.93 ppm (d) is assigned to the $CH_3$ group of the ligand. The broad signal near 3.99 ppm is assigned to $H^a$, whereas $H^b$ is observed at $\delta$ = 20.22 ppm. At 310 K, the methylene protons of the ethyl group, (c) and (c′), are observed at $\delta$ = 8.69 ppm and 7.73 ppm, respectively, with relative intensities of 1:1. Indeed the $Fe^{II}$ trischelate complex is chiral and these two protons are diastereotopic.[38a,38b] Notably, signals due to uncoordinated Et-bik ligand are always detectable in the NMR spectra of **2**.

In the spectrum of **3**, five signals of the vinyl-imidazole groups with the same intensity are observed at 310 K. The three vinylic protons are assigned according to their coupling constant value, considering that $J_{trans} > J_{cis} > J_{geminal}$ for the vinylic

system. The two doublets at $\delta$ = 7.20 ppm (d) and 5.89 ppm (e) are attributed to $H^d$ and $H^e$, respectively, whereas $H^c$ appears as doublet of doublets (dd) near 9.55 ppm. The strongly shifted signal observed at $\delta$ = 16.46 ppm is ascribed to $H^b$ (as for **1** and **2**) and the broad $H^a$ signal is observed at $\delta$ = 5.17 ppm.

### *Variable-Temperature $^1$H NMR Spectroscopic Studies*

The variable-temperature $^1$H NMR spectroscopic studies were carried out in the 230–350 K temperature range.[39] The spectra of **1**–**3** exhibit strong temperature dependence (Figure 6 and the Supporting Information). While the $^1$H chemical shifts are similar to those of the corresponding free ligands at 230 K, they strongly increase upon heating, spanning over 30 ppm at 350 K. This clearly accounts for a spin-state change from a diamagnetic LS state to a paramagnetic HS state upon heating. The increase of the signal half-width upon heating is also coherent with the occurrence of a paramagnetic state at high temperature. In contrast, the chemical shifts in compound **4** remain strongly shifted in all of the probed temperature range, but they tend to decrease significantly as the temperature increases (see the Supporting Information), following the typical behaviour of paramagnetic species. More specifically, the observed $\delta \times T$ versus $T$ curves vary linearly for all protons, showing that the high-spin model for complex **4** follows the Curie law in the explored temperature range (see the Supporting Information).

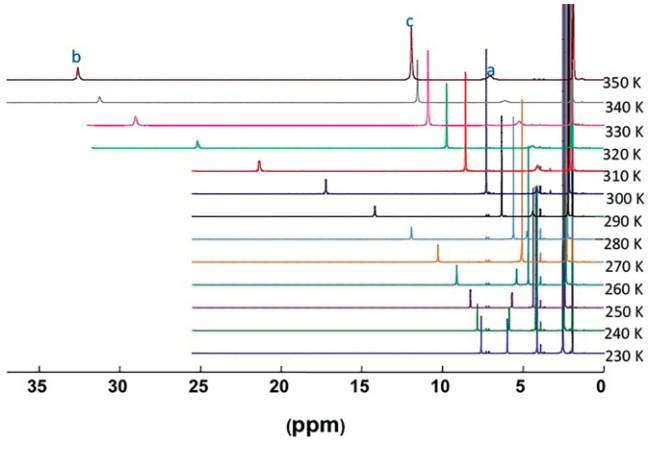


Figure 6. $^1$H NMR spectra of $[Fe(Me\text{-}bik)_3](BF_4)_2$ (**1**) in $CD_3CN$ in the temperature range 230–350 K.

The measured paramagnetic chemical shift, $\delta_{para}{}^T = \delta_{PC}{}^T + \delta_{FC}{}^T$, reflects the magnetic susceptibility of the complex [see Equations (3)–(6)]. Therefore the temperature dependence of the paramagnetic signals can be conveniently used to follow the thermal population of the HS state (see above). Indeed, the plots of $\delta_{para}{}^T(H^b) \times T$ versus temperature for **1**–**3** possess sigmoidal shapes, which is typical of spin-crossover complexes (Figure 7). Here, we selected the $H^b$ protons, which display a sharp signal and exhibit the highest chemical shift variation with temperature, to investigate the spin equilibria in **1**–**3** with more accuracy. It is also far enough from the paramagnetic centre (above 5 Å) to lead to a reduced dipolar contribution (proportional to $r^{-3}$). All of the other protons in these three complexes, except for $H^a$, exhibit the same trend and sigmoidal curves can be similarly obtained (see simulation in the Supporting Information). In the case of $H^a$, the chemical shift first slightly decreases, then increases, as the temperature increases. Here, the $Fe^{II}$–$H^a$ distance is short, ca. 3 Å; this likely leads to a stronger pseudocontact shift, which may induce some deviation from the Curie law if the contact term is small.

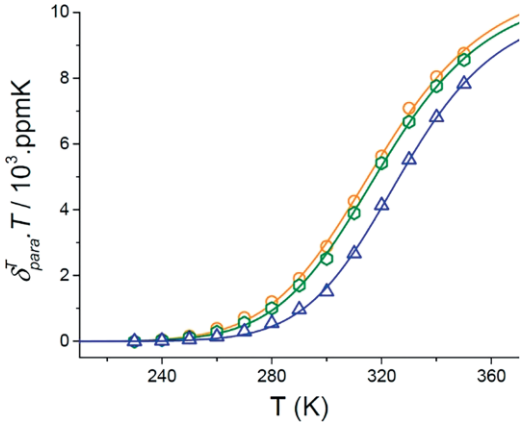


Figure 7. Thermal variation of the $\delta \times T$ product for the $H^b$ protons of the three complexes (**1**: orange circles; **2**: green circles; **3**: blue triangles) obtained from the variable-temperature $^1$H NMR spectroscopic study. The straight lines represent the simulated data (see text).

The comparison of the three curves shows that the change in the peripheral R group on the ligand has only a weak influence on the transition temperature. The temperature dependence of these chemical shifts can be modelled to extract the thermodynamic parameters of the Boltzmann spin equilibrium by using the following equation:[40]

$$\delta^T_{obs} \times T = \delta_{LS} \times T + \frac{C}{\left\{1+exp\left[\frac{\Delta H^\circ}{R}\left(\frac{1}{T}-\frac{1}{T1/2}\right)\right]\right\}} \quad (7)$$

where $\delta_{obs}{}^T$ is the experimental chemical shift and $\delta_{LS/dia}$ is the chemical shift in the diamagnetic state. The values extracted from these fits are given in Table 4. We assume that compounds **1**–**3** show a Curie-like behaviour as observed in the high-spin $Fe^{II}$ model compound **4** (see the magnetic and NMR spectroscopic data). The transition temperatures obtained from the $\delta_{para}{}^T(H^b) \times T$ versus $T$ plot are close to each other and are in

Table 4. Estimates of the thermodynamic parameters of the spin equilibria in **1**–**3** obtained from susceptibility measurements in solution using the regular solution model (ca. $10^{-2}$ mol $L^{-1}$).[36,46]

| Compound | VT $^1$H NMR | | | Evans method | | | Magnetometry | | |
|---|---|---|---|---|---|---|---|---|---|
| | $\Delta H_{HL}$ [kJ mol$^{-1}$] | $\Delta S_{HL}$ [J mol$^{-1}$ K$^{-1}$] | $T_{1/2}$ [K] | $\Delta H_{HL}$ [kJ mol$^{-1}$] | $\Delta S_{HL}$ [J mol$^{-1}$ K$^{-1}$] | $T_{1/2}$ [K] | $\Delta H_{HL}$ [kJ mol$^{-1}$] | $\Delta S_{HL}$ [J mol$^{-1}$ K$^{-1}$] | $T_{1/2}$ [K] |
| **1** | 41 | 128 | 319 | 38 | 118 | 323 | 35 | 106 | 328 |
| **2** | 43 | 134 | 320 | 44 | 119 | 326 | 42 | 126 | 328 |
| **3** | 45 | 136 | 329 | 44 | 118 | 332 | 42 | 123 | 337 |

the 319–330 K temperature range. The thermodynamic values are of the same order as those found in the solid state and they compare with those obtained by other techniques below.

Interestingly, the variable-temperature NMR spectroscopic study also reveals unusual behaviour for the diastereotopic $CH_2$ protons in compound **2**: these protons are distinguishable in an intermediate temperature range, 270–310 K, but they overlap at $T < 270$ K and $T > 310$ K. In the low temperature range (230–260 K), the complex is diamagnetic. The chemical-shift range is moderate (0–12 ppm) and the separation between the signals is small, so that only one peak is observed at 7.1 T. The use of a higher magnetic field (ca. 14 T) is necessary to reveal the presence of the diastereotopic protons at low temperatures (Figure 8).

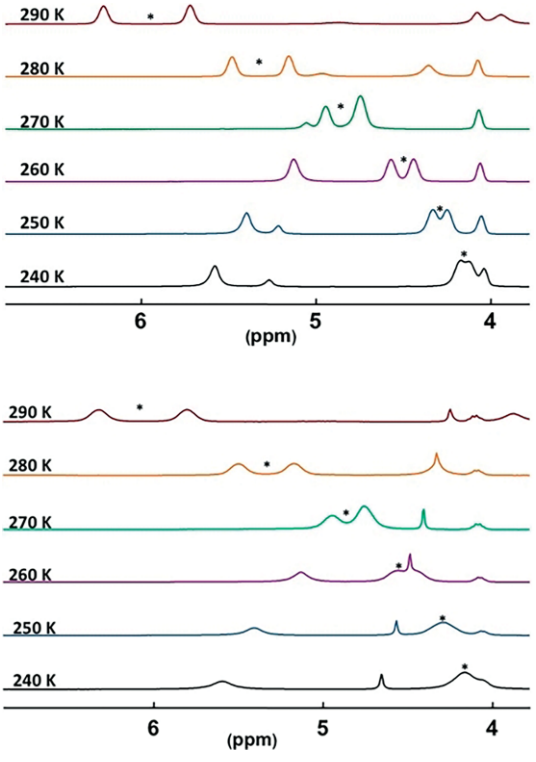


Figure 8. $CH_2$ diastereotopic signals (*) in **2** obtained from $^1$H NMR spectroscopy at 300 MHz and 600 MHz.

Upon heating, compound **2** becomes paramagnetic, the chemical-shift range is significantly broadened and the separation between the protons gradually increases from 230 K to 310 K. Although there is some signal broadening upon heating, the resolution is overall improved and the diastereotopic signal can be resolved. This effect is typical of paramagnetic species: the presence of small spin density delocalized on the probed nuclei allows spreading of the NMR spectroscopic chemical shift range and leads to a "magnifying glass effect".[41] The resolution improves many-fold and it can be even better than that obtained by using an high external magnetic field. Finally, at higher temperatures (above 310 K), coalescence occurs (see the Supporting Information), indicating the occurrence of a rapid chemical exchange between the two diastereotopic protons. This is due to a rapid isomerization of the Δ and Λ enantiomers, relative to the NMR spectroscopic measurement time.

## Magnetic Susceptibility Measurements through the Evans NMR Spectroscopic Method and SQUID Magnetometry

The magnetic susceptibility was measured by the Evans NMR spectroscopic method and SQUID magnetometry on acetonitrile solutions of the paramagnetic complexes **1**–**3** ($10^{-2}$ mol $L^{-1}$).[42] In the Evans experiments, the solutions were placed in an inner narrow-bore tube of a double-walled NMR spectroscopic tube. The difference between the solvent signal ($\Delta\upsilon$ in Hz) of a pure acetonitrile solution (outer tube) and the solvent signal of the paramagnetic solutions (inner tube) is proportional to the bulk magnetic mass susceptibility:[43]

$$\chi = \frac{3\Delta\upsilon}{4\pi\upsilon m} + \chi_0 + \frac{\chi_0(d_0 - d_s)}{m} \quad (8)$$

where $\chi$ is the mass paramagnetic susceptibility, $\upsilon$ is the operating radio frequency of the spectrometer ($3 \times 10^8$ Hz), $m$ is the concentration of the paramagnetic ion in the inner tube in g $cm^{-3}$, $\chi_0$ is the gram susceptibility of pure $CD_3CN$ solvent ($-0.534 \times 10^{-6}$ g $cm^{-3}$)[42] and $d_0$ and $d_s$ are the density of the pure solvent and the paramagnetic solution, respectively.[44] For strongly paramagnetic substances, the last term is often neglected, so that the mass susceptibility becomes:

$$\chi = \frac{3\Delta f}{4\pi f m} + \chi_0 \quad (9)$$

The molar susceptibility $\chi_M$ is calculated from $\chi$ in the usual way, taking into account the diamagnetic contribution calculated from the Pascal tables.[45]

Because of solvent evaporation from the double-walled Evans tube, the explored temperature range was limited to 230–330 K. As shown in Figure 9, a gradual increase of the $\chi_M \times T$ product is observed upon heating, in agreement with the occurrence of a SCO process in solution. The transition starts at ca. 280 K and is incomplete at the highest available temperature. At 330 K, the measured $\chi_M \times T$ product of **1**, **2** and **3** are 2.15, 2.24 and 1.64 $cm^3$ $mol^{-1}$ K, respectively. In contrast with the temperature-dependent $^1$H NMR spectroscopic experiment described above, the limited temperature range does not allow an accurate determination of the values of the spin-equilibrium transition, $T_{1/2}$. In the case of **2**, the magnetic susceptibility of the solution is particularly high at low temperature and accounts for the presence of a paramagnetic side product. This paramagnetic species has a fast relaxation, as it is not detected by $^1$H NMR spectroscopy (see above). As the only side product observed in the spectrum of **2** is the free Et-bik ligand, the paramagnetic side product is likely the high-spin $[Fe^{II}(Et\text{-}bik)_2(CH_3CN)_2](BF_4)_2$ complex, which is indeed NMR spectroscopically silent (the complex prepared in situ does not exhibit any signals). A partial dissociation of the $[Fe^{II}(R\text{-}bik)_3](BF_4)_2$ complex would thus occur in the case of **2**.

The SQUID magnetometry measurements confirm the results obtained by the Evans method (Figure 9). The $\chi_M \times T$ versus $T$ curves measured on the acetonitrile solutions of **1**–**3** (in the temperature range 220–350 K and under a 1 T magnetic field) exhibit shapes similar to those found by using the Evans method and they are in agreement with the occurrence of spin-

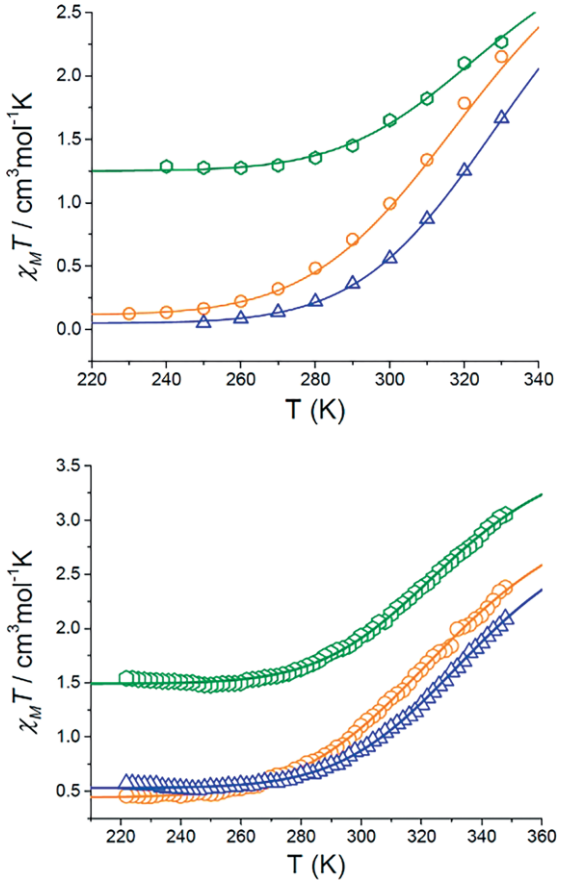


Figure 9. Thermal dependence of the $\chi_M \times T$ product for **1** (orange circles), **2** (green circles) and **3** (blue triangles) obtained from susceptibility measurements in $CD_3CN$ by using the Evans NMR spectroscopic method (top) and a SQUID magnetometer (bottom). The straight lines represent the simulated data (see text).

equilibria (starting from ca. 280 K and incomplete at 350 K). The $\chi_M \times T$ products for **1**, **2** and **3**, measured at 330 K (2.00, 2.64 and 1.61 cm$^3$ mol$^{-1}$ K, respectively), compare quite well with those found by the Evans method at the same temperature. The presence of a paramagnetic species in the solution of **2** at low temperature is also confirmed by these measurements.

These magnetic data were fitted by using a simple solution model:[46,47]

$$ln\frac{1-n_{HS}}{n_{HS}} = \frac{\Delta H}{RT} - \frac{\Delta S}{R} \quad (10)$$

The amount of HS complex, $n_{HS}$, or its relative fraction, $\gamma_{HS}$, is extracted from the equation:

$$\gamma_{HS}^{T} = \frac{(\chi_M T)_T - (\chi_M T)_{LT}}{(\chi_M T)_{HT} - (\chi_M T)_{LT}} \quad (11)$$

where $(\chi_M \times T)$ is the value of the product $(\chi_M \times T)$ at any temperature. The $(\chi_M \times T)_{LT}$ and $(\chi_M \times T)_{HT}$ correspond to the value of $(\chi_M \times T)$ at low temperature and high temperature, respectively.

The thermodynamic parameters are finally obtained by fitting the equation:

$$(\chi_M T)_T = (\chi_M T)_{LT} + \frac{(\chi_M T)_{HT} - (\chi_M T)_{LT}}{1+exp\left[\frac{\Delta H^\circ}{R}\left(\frac{1}{T} - \frac{1}{T_{1/2}}\right)\right]} \quad (12)$$

The simulations of the curves lead to similar values (Table 4) and are in qualitative agreement with those found by other techniques (see comments below).

The results obtained from the Evans method, the direct measurement of the magnetic susceptibility in solution and the $^1$H NMR spectroscopic study lead to coherent results. The transition temperatures, $T_{1/2}$, remain close to each other for the three techniques (319–335 K). The values obtained for the vinyl-bik derivative, **3**, seem to be slightly higher (in all cases) than those measured for **1** and **2**. Overall, the modification of the R group does not have a strong influence on the spin equilibrium in solution. This contrasts with the situation in the solid state, where small interactions (CH–π) seem to significantly affect the $T_{1/2}$ ($\Delta T_{1/2}$ = 65 K).

The thermodynamic parameters obtained for the three compounds are unusually high, but they are coherent within the three techniques. They are also similar to the values obtained in the solid state, where gradual transitions are observed. The VT NMR spectroscopic study ($\delta \times T$ versus $T$ measurement) appears to be more accurate over magnetometry techniques (SQUID magnetmetry or Evan's method), as small changes in the magnetic state of the probed complex can be reflected by important modifications in the chemical shifts. For instance, the chemical-shift variation, observed in the $^1$H NMR spectra at various temperatures, in the SCO complex are much more important than those observed in the solvent in the Evans method. Moreover, the VT $^1$H NMR spectroscopy allows the selective probing of the SCO complex. Indeed, the presence of paramagnetic impurities would bring more error sources in the magnetometry measurements. Here, the thermodynamic values deduced by directly probing an adequately chosen proton in **2** validate the estimated values obtained in magnetometry (where both compound **2** and a side product are measured).

Overall, the more pronounced sigmoidal curve is obtained from the variable-temperature NMR spectroscopic study. The main advantage of this technique in comparison with the others is the following: the possible presence of other species does not interfere with the measurement, as the physical value measured is a selected chemical shift of the SCO complex, which directly reflects its magnetic state.

## Computational Studies

To gain further insights into the electronic structure and magnetic properties of complexes **1**–**4**, we have undertaken density functional calculations using density functional theory (see Exp. Sect.). The spin-state splitting of Fe$^{II}$ complexes that exhibit SCO properties are challenging for several exchange-correlation functionals; in particular, functionals such as B3LYP*,[48] OPBE[49] and B3LYP[50] have been recommended for the computation of spin-state splitting. Due to considerably greater HF exchange (20 % in B3LYP), a hybrid functional, such as B3LYP, tends to weaken the M–L bonds, which stabilize the HS state, compared with the LS state. On the other hand, dispersion and solvent

effects shorten the M–L bonds which increase the bond-dissociation energies and therefore favour the LS state. Here, we have optimized complexes **1**–**4** using the B3LYP* and OPBE functionals, with the incorporation of dispersion correction, as recommended by Grimme,[51] and solvent effects, as suggested earlier.[52] The computed energies using these functionals suggest the LS state as the ground state for the B3LYP* and OPBE functionals; the estimated HS–LS gaps are 31.0, 37.2, 33.2 and 5.99 kJ mol$^{-1}$ for complexes **1**–**4**, respectively, using the OPBE functional, whereas the B3LYP* functional yields 98.3, 73.4, 102.0 and 82.7 kJ mol$^{-1}$ for complexes **1**–**4**, respectively. The optimized energies computed using B3LYP, on the other hand, reveal the high-spin state as being the ground state for all of the complexes, with the energy difference between the HS and LS states being 8.8, 6.0 and 6.1 kJ mol$^{-1}$ for complexes **1**–**3**, respectively. For complex **4**, on the other hand, calculations reveal a HS–LS gap of 20.7 kJ mol$^{-1}$, more than twice the value observed for other complexes. Although the B3LYP* and OPBE functionals clearly suggest the LS ground state for **1**–**3**, the ground state predicted for complex **4** is contrary to that found by experiment. However, the energy difference obtained from the OPBE and B3LYP* functionals are very large and suggest, in fact, that the SCO feature is not possible. The energies computed using B3LYP, on the other hand, are small and clearly suggest SCO features, and therefore, here we have elaborated the discussion on the structure and bonding using this functional. Besides, theoretical studies on a series of {Fe$^{II}$N6} SCO complexes by various functionals suggests that although B3LYP fails to predict correct spin ground state multiplicity, the overall order of the HS–LS energy differences for a group of structurally related compounds are better described. For these reasons, here, we intend to employ B3LYP computed data for further discussion.[50]

The computed geometry for **1**–**4** in their LS and HS states are given in Figure 10 and the structural parameters are summarized in Table 5 for all three functionals. Here, we discuss, in detail, the geometry computed using B3LYP. Calculations clearly reveal that in all four cases, the Fe–N distances in the LS states are in the range of 2.03 to 2.05 Å, while at the HS surface, the bond lengths are in the range of 2.22 to 2.25 Å. The structural distortion is also quite significant in the high-spin geometry. The complex **4** exhibits the longest average Fe–N bond lengths and the maximum octahedral distortions among all of the four computed complexes, in agreement with the single-crystal X-ray diffraction structure and CShM analysis (see above). The distortions within the ligand geometry and twists in the planarity of the imidazole rings are also reflected in the optimized structures. The nature of the spin ground state is determined by the orbital splitting and the spin-pairing energy. For complexes **1**–**4**, calculations yield the following electronic configuration $(d_{xz})^2(d_{yz})^1(d_{xy})^1(d_{x^2-y^2})^1(d_{z^2})^1$ for the high-spin configuration.

To gain further insights into the nature of the bonding, we have plotted the d-based orbitals of complexes **1** and **4** (Figure 11). The presence of the ketone group in **1**–**3** promotes delocalization of the π clouds between the two imidazole rings, leading to stronger donor ability, and thus, a stabilization of the LS state. This feature is absent in complex **4**, as depicted in

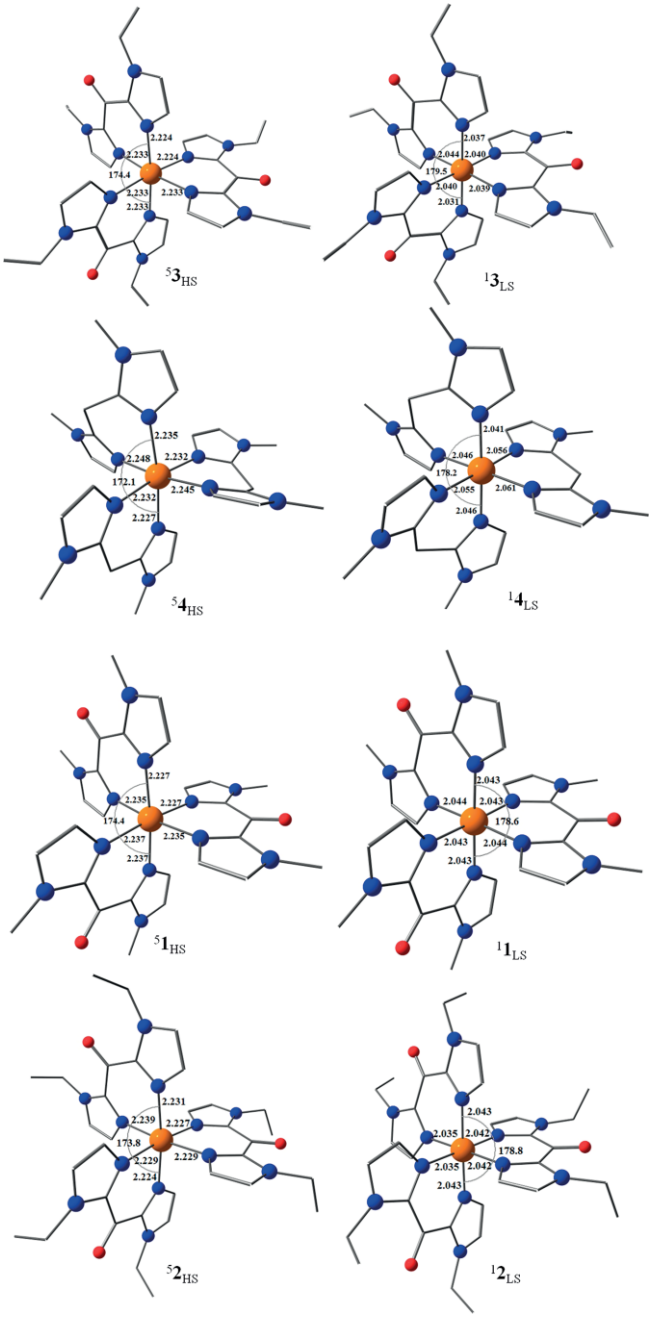


Figure 10. B3LYP computed optimized HS and LS geometries for **1**–**4**. Colour code: orange: Fe; blue: N; red: O; grey: C. Hydrogen atoms are omitted for clarity.

Figure 11. The orbital splitting $\Delta E(d_{xz} - d_{z^2})$ is estimated to be 1.476 eV, 1.450 eV and 2.438 eV for complexes **1**–**3**, respectively. The close splitting pattern observed for complexes **1** and **2** is consistent with the similar $T_{1/2}$ values measured in solutions, while the relatively larger splitting pattern computed for complex **3** is in agreement with better stabilization of the LS state up to ca. 335 K (see above). The participation of the vinyl π orbital leads to a stronger interaction of the ligands with the $d_{xz}/d_{yz}$ orbitals and to larger orbital splitting and stabilization of the LS state (see the Supporting Information for eigenvalue plots of complexes **1**, **2** and **4**). This nicely correlates with the experimental results, as **3** exhibits a higher $T_{1/2}$ than **1** and **2**.

Table 5. B3LYP-, OPBE- and B3LYP*-optimized selected bond and angle parameters for complexes **1**–**4**.

| B3LYP | | | | | | | | |
|---|---|---|---|---|---|---|---|---|
| Bonds and angles | Complex **1** | | Complex **2** | | Complex **3** | | Complex **4** | |
| | HS | LS | HS | LS | HS | LS | HS | LS |
| Fe–N1 [Å] | 2.226 | 2.043 | 2.229 | 2.034 | 2.233 | 2.040 | 2.248 | 2.055 |
| Fe–N2 [Å] | 2.237 | 2.043 | 2.231 | 2.042 | 2.224 | 2.038 | 2.235 | 2.046 |
| Fe–N3 [Å] | 2.234 | 2.044 | 2.227 | 2.043 | 2.232 | 2.037 | 2.232 | 2.040 |
| Fe–N4 [Å] | 2.237 | 2.043 | 2.239 | 2.042 | 2.233 | 2.039 | 2.245 | 2.055 |
| Fe–N5 [Å] | 2.227 | 2.044 | 2.224 | 2.034 | 2.232 | 2.044 | 2.226 | 2.061 |
| Fe–N6 [Å] | 2.234 | 2.043 | 2.229 | 2.043 | 2.224 | 2.031 | 2.232 | 2.046 |
| N3–Fe–N6 [°] | 174.4 | 178.6 | 173.8 | 178.8 | 174.4 | 179.5 | 172.1 | 178.2 |
| $\varrho$(Fe)[a] | 3.88 | 0.00 | 3.83 | 0.00 | 3.87 | 0.00 | 3.89 | 0.00 |
| OPBE | | | | | | | | |
| Bonds and angles | Complex **1** | | Complex **2** | | Complex **3** | | Complex **4** | |
| | HS | LS | HS | LS | HS | LS | HS | LS |
| Fe–N1 [Å] | 2.130 | 1.942 | 2.113 | 1.919 | 2.136 | 1.929 | 2.150 | 1.938 |
| Fe–N2 [Å] | 2.128 | 1.923 | 2.132 | 1.938 | 2.121 | 1.918 | 2.158 | 1.931 |
| Fe–N3 [Å] | 2.132 | 1.935 | 2.122 | 1.947 | 2.131 | 1.941 | 2.176 | 1.958 |
| Fe–N4 [Å] | 2.128 | 1.935 | 2.122 | 1.947 | 2.135 | 1.944 | 2.157 | 1.958 |
| Fe–N5 [Å] | 2.124 | 1.923 | 2.133 | 1.938 | 2.113 | 1.925 | 2.144 | 1.931 |
| Fe–N6 [Å] | 2.132 | 1.942 | 2.113 | 1.919 | 2.132 | 1.935 | 2.155 | 1.938 |
| N3–Fe–N6 [°] | 177.6 | 179.7 | 178.9 | 174.9 | 176.6 | 179.5 | 177.4 | 179.9 |
| $\varrho$(Fe)[a] | 3.91 | 0.00 | 3.91 | 0.00 | 3.92 | 0.00 | 3.78 | 0.00 |
| B3LYP* | | | | | | | | |
| Bonds and angles | Complex **1** | | Complex **2** | | Complex **3** | | Complex **4** | |
| | HS | LS | HS | LS | HS | LS | HS | LS |
| Fe–N1 [Å] | 2.147 | 1.978 | 2.155 | 1.963 | 2.147 | 1.974 | 2.168 | 1.990 |
| Fe–N2 [Å] | 2.136 | 1.965 | 2.133 | 1.976 | 2.130 | 1.958 | 2.149 | 1.976 |
| Fe–N3 [Å] | 2.138 | 1.980 | 2.129 | 1.984 | 2.139 | 1.976 | 2.146 | 1.996 |
| Fe–N4 [Å] | 2.149 | 1.980 | 2.126 | 1.984 | 2.136 | 1.977 | 2.147 | 1.990 |
| Fe–N5 [Å] | 2.139 | 1.965 | 2.126 | 1.976 | 2.126 | 1.962 | 2.150 | 1.970 |
| Fe–N6 [Å] | 2.141 | 1.978 | 2.162 | 1.963 | 2.145 | 1.978 | 2.187 | 1.984 |
| N3–Fe–N6 [°] | 176.7 | 179.7 | 169.9 | 176.0 | 175.2 | 179.4 | 169.9 | 179.1 |
| $\varrho$(Fe)[a] | 3.78 | 0.00 | 3.79 | 0.00 | 3.79 | 0.00 | 3.68 | 0.00 |

[a] Spin density on the Fe.

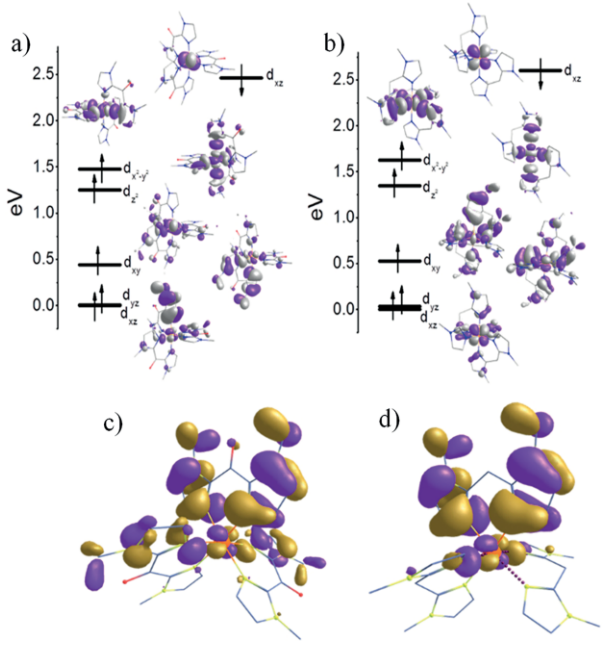


Figure 11. Energy splitting of d-based orbitals for: (a) complex **1**; and (b) complex **4**. Molecular orbital (MO) diagram showing the presence of a more extended π-interaction in complex **1** (c) than in complex **4** (d).

Besides, significant C–H···O interactions are detected between the alkyl/vinyl hydrogen and the ketone oxygen atoms in complexes **1**–**3**.[53] The strength of this interaction varies within the set of complexes **1**–**3**, in line with the C–H···O distances, which are 2.55, 2.30 and 2.26 Å for complexes **1**, **2** and **3**, respectively. This interaction is found to weaken the donor abilities of the imidazole ring; however, its effect remains small and does not compensate the dominant π-acceptor contribution that leads to the stronger ligand field in the vinyl complex.

This is also supported by the computed spin densities where complexes **1**–**3** possess a net spin density of 3.888 at the Fe atom for the HS spin state, while complex **4** has slightly higher spin density at the Fe atom (3.890). Computed spin-density plots of complexes **1** and **4** are shown in Figure 12. The spin density at the metal centre has an octahedral shape and is partially delocalized onto the ligands. The nitrogen atom coordinated to the Fe centre in complex **1** has a spin density in the range of 0.021–0.023, while the corresponding atom in complex **4** spans the range 0.016–0.026. The oxygen atom of the ketone group also exhibits some spin densities in complexes **1**–**3**. Although the quoted values are small, the differences observed clearly indicate significant structural and electronic alteration upon ligand modifications, leading to variations in the SCO properties.

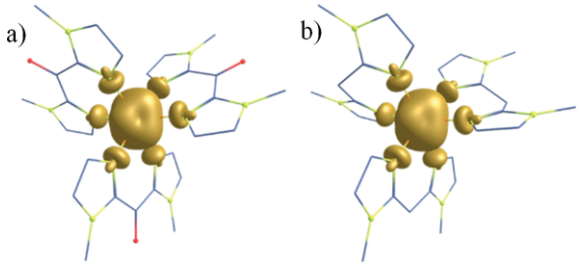


Figure 12. B3LYP-computed spin densities for (a) complex **1**; and (b) complex **4** in their high-spin states.

To evaluate the parameters that are correlated to the spin-crossover properties, we have estimated the $\Delta S$ and $T_{1/2}$ values for complexes **1**–**3**.

The $T_{1/2}$ can be computed from the electronic energy and the vibrational and entropic contributions to the energy by using the following equation, as advocated earlier:[54]

$$T_{1/2} = \left[\Delta E_{el}(0) + \Delta E_{vib}\left(T_{\frac{1}{2}}\right)\right] / \Delta S\left(T_{\frac{1}{2}}\right) \quad (13)$$

where $\Delta E_{el}(0)$ is the electronic energy difference between the high-spin and low-spin states, along with the zero-point-energy correction and the thermal correction to the electronic energy; $\Delta E_{vib}$ is the vibration due to thermal energy and $\Delta S$ is the entropy of the system.

The vibrational and entropic contributions are estimated from frequency calculations, as discussed in the Exp. Sect. The $\Delta S$ values are estimated to be 59.6, 53.4 and 36.7 J K$^{-1}$ mol$^{-1}$ for complexes **1**–**3**, respectively (see Table 6). These values are small, compared with the experimental ones, but they do not take into account a possible conformational change in the ligand upon spin-state change, as discussed above. On the other hand, the $\Delta E_{vib}$ values are estimated to be –0.8, –1.4 and –2.2 kcal mol$^{-1}$ for complexes **1**–**3**, respectively. The estimated $T_{1/2}$ values, 308.5, 277.1 and 438.5 K for complexes **1**–**3**, respectively, are different from the experimental ones, but the largest value computed for complex **3** is consistent with the observed trend in the experiments.

Table 6. Estimates of the thermodynamic parameters of the spin equilibria estimated using DFT calculations for complexes **1**–**3**.

| Compounds | $\Delta H_{SCO}$ [KJ mol$^{-1}$] | $\Delta S_{SCO}$ [J mol$^{-1}$ K$^{-1}$] | $T_{1/2}$ [K] |
|---|---|---|---|
| [Fe(Me-bik)$_3$] (BF$_4$)$_2$ | 25.6 | 59.6 | 308.5 |
| [Fe(Et-bik)$_3$] (BF$_4$)$_2$ | 22.8 | 53.4 | 277.1 |
| [Fe(V-bik)$_3$] (BF$_4$)$_2$ | 25.6 | 36.7 | 438.5 |

## Conclusion

In this work, we have studied, both in the solid state and in solution, the SCO phenomenon of closely related [Fe$^{II}$(R-bik)$_3$]$^{2+}$ complexes containing similar β-diimine ligands. Our goal was to evaluate the influence of the ligand functionalization over the switching properties of these systems. The results from the DFT calculations were also compared with the experimental results, with the aim of rationalizing the magnetic properties.

The theoretical calculations, based on density functional methods, have been performed for all four complexes and the employed methodology gave a satisfying description of both the structure and electronic properties of these complexes. The computed energy differences between the HS and LS structures rationalize the presence of SCO properties in complexes **1**–**3**. The theoretical calculations permit the clarification of the critical role of the central ketone group on the magnetic and optical properties of the studied complexes. The computed electronic structures and spin densities revealed that the C=O group in complexes **1**–**3** favour π delocalization between the two imidazole rings. This leads to an enhancement of the ligand π-acidic character, and therefore, an increase of the ligand field strength, leading to the stabilization of the LS state as the ground state. Indeed, whereas the [Fe$^{II}$(bim)$_3$]$^{2+}$ model complex remains high spin, the derivative complexes containing the α-keto-β-diimine ligands exhibit stronger ligand fields and show SCO behaviour near room temperature.

The R groups in the R-bik ligands were shown to have a moderate influence on the $T_{1/2}$ measured in solution. The inductive attractive group (vinyl) was expected to reduce the ligand field and stabilize the high-spin state; that is, leading to a decrease of the $T_{1/2}$. Conversely, inductive donor groups (ethyl and methyl) were expected to lead to an increase of the $T_{1/2}$. The observed trend is the opposite and tends to show that the vinyl group contributes to the delocalization of the π-system, leading to a higher π-acidic character and a stronger ligand field. The DFT-computed MO diagram highlights this point, as stronger interactions of the ligands with $d_{xz}/d_{yz}$ orbitals are detected. The differences remain, however, moderate, with $T_{1/2}$ increasing by 10–15 K from the donor alkyl to the attractive vinyl group. The weak C–H···O between the alkyl/vinyl and ketone groups may also influence the ligand field induced by these ligands. The interaction is found to be stronger in the case of the vinyl-bik ligand, but its effect remains apparently moderate.

To analyse the spin-crossover process in solution, we used three different methods, including the Evans NMR spectroscopic method. This technique gives access to the bulk susceptibility of the solution, so if paramagnetic side-product(s) are present in solution (or if chemical exchange occurs), the measurement can lead to ambiguous results, as illustrated in compound **2**. Bulk susceptibility was also extracted from measurements in solution by using SQUID magnetometry. Although the SQUID technique is more sensitive than the Evans method (more highly diluted solutions can be studied), it suffers from similar inconveniences. Overall, in the present experimental conditions, the best SCO equilibrium curves (with the most pronounced sigmoidal shape) are obtained from the NMR spectroscopic study. By tracking the temperature dependence of an adequately chosen $^1$H chemical shift (which bears a strong contribution from the Fermi contact term), we were able to follow the spin-crossover process of the three compounds. In this case, the possible presence of other paramagnetic species does not interfere with the measurements, since the physical value measured is a selected chemical shift of the SCO complex, which directly reflects its magnetic state. The thermodynamic values

$\Delta H$ and $\Delta S$ deduced from these measurements are high, but are coherent among the three techniques and are of the same order of magnitude for the three complexes. The high $\Delta S$ value is probably related to the change in the ligand conformation between the HS and LS state. Although it was not possible to obtain a crystal structure of the HS state (because of the loss of crystallinity), such changes in the ligand geometry were previously observed in other switchable molecules containing the R-bik ligand.[28]

Beside the study of the spin equilibrium, $^1$H NMR spectroscopy allowed us to study the stability of the species over the explored temperature range and the possible occurrence of chemical equilibrium, provided that the paramagnetic species have suitable NMR spectroscopic signals (i.e., convenient nuclear relaxation times). Interestingly, we were able to observe, in the case of compound **2**, an isomerization between the two $\Delta$ and $\Lambda$ stereoisomers. Whereas the two isomers cannot be detected at low temperature (since the signals are diamagnetic) unless high-field NMR spectroscopy is used, at higher temperatures, the presence of spin density on the probed nuclei leads to an enlargement of the chemical shift range and improved resolution (as long as coalescence does not occur).

Finally, variable-temperature susceptibility data were used to analyse the spin-transition process in the solid state and to extract the associated thermodynamic parameters. The spin-transition temperatures, which are close to each other in solution, are clearly spread in a broader temperature range in the solid state. They are close (316 K) in **1**, higher (342 K) in **3** and lower (277 K) in **2** than those measured in acetonitrile solution. The intermolecular interactions and the solid-state organization clearly affect the energetics of the system. Overall, the spin transitions remain gradual, with almost no cooperative effect, as only weak intramolecular interactions are observed in the structures of compounds **1**–**3**. In contrast with **1** and **2**, the transition observed for compound **3** is clearly affected by the loss of solvent molecules that occurs upon heating.

## Experimental Section

**Materials:** All chemicals and solvents were purchased from Sigma Aldrich and Alfa Aesar and were used as received. All of the experiments were carried out under aerobic conditions (except for the synthesis of compound **4**).

**Instrumentation:** FTIR spectra were recorded over the range 4000–400 cm$^{-1}$. Measurements were carried out with a Tensor 27 Bruker instrument working in the ATR mode (on fresh samples). Solid-state UV/Vis spectra were measured at room temperature with a PerkinElmer Lambda 1050 WB spectrophotometer. The measurements were performed on KBr pellets. Thermogravimetric analysis were carried out with a TGA analyzer (TA instrument, SDT Q600) at a rate of 2 °C min$^{-1}$ under $N_2$ flow (100 mL min$^{-1}$).

**Magnetic Studies:** Magnetic susceptibility data were collected with a Quantum Design SQUID magnetometer (MPMS-5S) calibrated against a standard palladium sample. The magnetic susceptibility values were corrected from the diamagnetism of the molecular constituents using Pascal's Table[45] and from the sample holder. The measurements in the solid state were carried out on polycrystalline samples of **1**–**4** in the temperature range 4–400 K in a 1 T magnetic field. The susceptibility measurements of solutions of **1**–**3** ($\times 10^{-2}$ mol L$^{-1}$) were carried out in the temperature range 220–350 K under an external magnetic field of 1 T. The rapid evaporation of $CH_3CN$ above 350 K, and its freezing below 220 K, prevented us from exploring a broader temperature range. Diamagnetic corrections were estimated by measuring the same amount of pure $CH_3CN$ solution in the same container. Photomagnetic measurements on fresh samples of **1**–**3** were carried out by using a sample holder equipped with an optical fibre. In a typical experiment, ground crystals (0.4 mg) were deposited on an adhesive tape. The sample was separated from the end of the fibre by ca. 5.5 cm. All of the irradiations were carried out at 20 K to minimize the temperature variation induced by the laser light.

**NMR Spectroscopic Studies:** The NMR spectra of **1**–**3** were recorded with a Bruker Avance$^{II}$ 300 spectrometer operating at a $^1$H Larmor frequency of 299.95 MHz and equipped with a BBMS variable-temperature unit. A variable-temperature NMR spectroscopic experiment was also carried out for **2** with a Bruker Avance$^{II}$ 600 spectrometer ($^1$H Larmor frequency of 600.13 MHz). The concentration of all three paramagnetic samples was $\times 10^{-2}$ mol L$^{-1}$ for all experiments. The spectra were collected over the 230–350 K temperature range (for variable-temperature $^1$H NMR spectroscopy) and 230–330 K (for the Evans NMR spectroscopic method). The observed signals were referenced using the solvent proton signal ($\delta$ = 1.94 ppm relative to TMS). The temperature was calibrated using the standard Wilmad methanol and ethylene glycol samples for low and high temperatures, respectively.

**Ligand Synthesis:** Ligands, including Me-bik [bis(1-methylimidazol-2-yl)ketone], Et-bik [bis(1-ethylimidazol-2-yl)ketone], V-bik [bis(1-vinylimidazol-2-yl)ketone], bim [bis(1-methylimidazol-2-yl)ketone], were prepared according to literature procedures.[55,56]

**Synthesis of Compounds 1–4**

**[Fe(Me-bik)$_3$](BF$_4$)$_2$·0.25H$_2$O (1) and [Fe(Et-bik)$_3$](BF$_4$)$_2$ (2):** Similar synthetic procedures were used for **1** and **2**. A colourless solution of Fe(BF$_4$)$_2$·6H$_2$O (169 mg, 0.5 mmol) in methanol (5 mL) was added to a methanolic (20 mL) solution of the ligand (Me-bik: 285 mg; Et-bik: 327 mg; 1.5 mmol). The resulting deep-blue solution was stirred for 30 min at room temperature and filtered. The compounds [Fe(Me-bik)$_3$](BF$_4$)$_2$·0.25H$_2$O and [Fe(Et-bik)$_3$](BF$_4$)$_2$ were obtained as dark platelike crystals after a few days of slow evaporation of the solution under ambient conditions. Yield: 77 % (**1**); 55 % (**2**).

**Compound 1:** $^1$H NMR (300 MHz, $CD_3CN$, 300 K): $\delta$ = 4.14 (s, 2 H, $H_{im}$), 7.29 (s, 6 H, $CH_3$), 17.22 (s, 2 H, $H_{im}$) ppm. ATR-IR (solid): $\tilde{\nu}$ = 3139.9, 2980.0, 1636.6, 1523.2, 1486.1, 1413.0, 1291.2, 1166.0, 1035.1, 896.9, 785.0, 769.3 cm$^{-1}$. $C_{27}H_{30.5}B_2F_8FeN_{12}O_{3.25}$ (804.57): calcd. C 40.31, H 3.82, N 20.89; found C 40.71, H 3.89, N 20.78. ESI-MS: calcd. for [Fe$^{II}$(Me-bik)$_3$]$^{2+}$ 313.10; found 313.30, calcd. for [Fe$^{II}$(Me-bik)$_2$(BF$_4$)]$^+$ 523.10; found 523.30, calcd. for [Fe$^{II}$(Me-bik)$_3$(BF$_4$)]$^+$ 713.40; found 713.60.

**Compound 2:** $^1$H NMR (300 MHz, $CD_3CN$, 300 K): $\delta$ = 4.12 (s, 2 H, $H_{im}$), 2.47 (s, broad, 6 H, $CH_3$), 16.02 (s, 2 H, $H_{im}$), 7.39 (s, broad, 2 H, $CH_2$), 6.72 (s, broad, 2 H, $CH_2$) ppm. ATR-IR (solid): $\tilde{\nu}$ = 3125.6, 2987.7, 1637.4, 1475.6, 1405.5, 1292.9, 1162.9, 1028.0, 890.8, 790.5, 769.6 cm$^{-1}$. $C_{33}H_{42}B_2F_8FeN_{12}O_3$ (884.22): calcd. C 44.83, H 4.79, N 19.01; found C 45.33, H 4.88, N 19.10. ESI-MS: calcd. for [(Et-bik) + H]$^+$ 219.21; found 219.30, calcd. for [(Et-bik) + Na]$^+$ 241.11; found 241.16, calcd. for [Fe$^{II}$(Et-bik)$_3$]$^{2+}$ 355.13; found 355.21, calcd. for [Fe$^{II}$(Et-bik)$_3$(BF$_4$)$_2$ + 2H]$^{2+}$ 443.16; found 443.27, calcd. for [(Et-bik)$_2$ + Na]$^+$ 459.40; found 459.28.

**[Fe(V-bik)$_3$](BF$_4$)$_2$·1.5H$_2$O (3):** A colourless solution of Fe(BF$_4$)$_2$·6H$_2$O (169 mg, 0.5 mmol) in a (4:1) mixture of acetonitrile/

water (5 mL) was added to a solution of V-bik (321 mg, 1.5 mmol) in the same solvent (20 mL) . The resulting blue solution was then stirred for 30 min at room temperature and filtered. $[Fe(V\text{-}bik)_3](BF_4)_2$ was obtained as dark platelike crystals after two weeks of slow evaporation of the solution under ambient conditions. Yield: 75 %.

**Compound 3:** $^1H$ NMR (300 MHz, $CD_3CN$, 300 K): $\delta$ = 5.37 (s, 2 H, $H_{im}$), 6.45 (d, 2 H, $CH_{vinyl}$), 12.88 (s, 2 H, $H_{im}$), 8.92 (dd, 2 H, $CH_{2vinyl}$), 5.78 (d, 2 H, $CH_{2vinyl}$) ppm. ATR-IR (solid): $\tilde{\nu}$ = 3139.4, 2982.0, 1643.1, 1472.9, 1425.7, 1315.6, 1278.0, 1157.6, 1033.7, 955.6, 891.4, 790.9, 765.6 $cm^{-1}$. $C_{33}H_{32}B_2F_8FeN_{12}O_{4.5}$ (898.14): calcd. C 44.08, H 3.70, N 18.69; found C 44.15, H 3.68, N 18.70. ESI-MS: calcd. for $[Fe^{II}(V\text{-}bik)_2]^{2+}$ 242.05; found 242.05, calcd. for $[Fe^{II}(V\text{-}bik)_3]^{2+}$ 349.10; found 349.09, calcd. for $[(V\text{-}bik)_2 + Na]^+$ 451.17; found 451.16, calcd. for $[Fe^{II}(V\text{-}bik)_3(BF_4)_3 + 2Na + H]^{2+}$ 503.09; found 503.10, calcd. for $[Fe^{II}(V\text{-}bik)_2(BF_4)]^+$ 571.11; found 571.11, calcd. for $[Fe^{II}(V\text{-}bik)_2(BF_4)(H_2O)(MeOH)]^+$ 621.15; found 621.15, calcd. for $[Fe^{II}(V\text{-}bik)_3(BF_4)]^+$ 785.23; found 785.20.

**$[Fe(bim)_3](OTf)_2$ (4):** A solution of $Fe^{II}(OTf)_2$·2MeCN (124 mg, 0.28 mmol) in dry THF (5 mL) was added dropwise to a stirred solution of bim ligand (150 mg, 0.85 mmol) in dry THF (10 mL) under an inert atmosphere. The resulting suspension was stirred at room temperature overnight. The white solid was then filtered and washed with THF (2× 10 mL). The layering of toluene with an acetonitrile solution of **4** gave colourless needlelike crystals within two days. Yield: 75 %. The compound has to be stored in an oxygen-free medium to avoid the oxidation of the ligand that leads to the formation of the $[Fe(Me\text{-}bik)_3]^{2+}$ complex.

**Compound 4:** $^1H$ NMR (400 MHz, $CD_3CN$, 300 K): $\delta$ = 0.87 (s, 2 H, $CH_2$), 12.63 (s, 6 H, $CH_3$), 39.70 (s, 2 H, $H_{im}$), 43.69 (s, 2 H, $H_{im}$) ppm. ATR-IR (solid): $\tilde{\nu}$ = 3134.6, 2959.0, 1541.2, 1508.0, 1412.3, 1327.5, 1262.1, 1148.1, 1124.0, 1031.4, 955.9, 754.1, 747.2 $cm^{-1}$. $C_{29}H_{36}F_6FeN_{12}O_6$ (818.52): calcd. C 39.46, H 4.11, N 19.04, S 7.13; found C 39.37, H 4.21, N 18.64, S 7.13.

**X-ray Diffraction Crystallography:** A single crystal of each compound was selected, mounted and transferred into a cold nitrogen gas stream. Intensity data was collected with Bruker Kappa-APEX2 systems using micro-source Cu-$K_\alpha$ (**1**, **3**, **4**) or fine-focus sealed tube Mo-$K_\alpha$ (**2**) radiations. Unit-cell parameter determinations, the data collection strategy, integration and absorption corrections were carried out with the Bruker APEX2 suite of programs. The structures were solved using SIR92[57] (**1**, **2**), SHELXS-86[58] (**3**) and Superflip[59] (**4**) and were refined anisotropically by full-matrix least-squares methods using SHELXL2014[60] within the WinGX[60] suite (**1**, **2**) or CRYSTALS[61] (**3**, **4**). Crystallographic details are given in Table S1.

CCDC 1481941 (for **1**), 1481942 (for **2**), 1481943 (for **3**) and 1481944 (for **4**) contain the supplementary crystallographic data for this paper. These data can be obtained free of charge from The Cambridge Crystallographic Data Centre.

**Computational Studies:** DFT[62] calculations were performed on the X-ray diffraction structural coordinates using the Gaussian 09[63] for all four complexes. Calculations were performed in two steps: (i) optimization of the nuclear coordinates of the single-crystal X-ray diffraction structure; and (ii) extraction of the thermodynamic parameters from frequency calculations based on the optimized coordinates. All calculations employed Becke's exchange functional,[64] together with the correlation functional of Lee, Yang and Parr[65] (B3LYP as implemented in Gaussian), along with Ahlrichs polarized triple-ζ valence (TZVP)[66] basis set for the metal ion and Pople's split valence polarized 6-31G**[67] basis set for rest of the atoms.

## Acknowledgments

This work was also supported by the Ministère de l'Enseignement et de la Recherche, and the Centre National de la Recherche Scientifique.

**Keywords:** Spin crossover · Iron · β-Diimine ligand · Paramagnetic NMR spectroscopy · Density functional calculations

[1] a) F. Benito-Lopez, R. Byrne, Y. Wu, L. Nolan, J. Kim, K. T. Lau, G. G. Wallace, D. Diamond, *ECS Trans.* **2009**, *19*, 199–210; b) S. Cobo, G. Molnár, J. A. Real, A. Bousseksou, *Angew. Chem. Int. Ed.* **2006**, *45*, 5786–5789; *Angew. Chem.* **2006**, *118*, 5918.
[2] a) C.-J. Fang, Z. Zhu, W. Sun, C.-H. Xu, C.-H. Yan, *New J. Chem.* **2007**, *31*, 580–586; b) M.-D. Ward, *J. Chem. Educ.* **2001**, *78*, 321–328.
[3] a) O. Kahn, J.-P. Launay, *Chemtronics* **1988**, *3*, 140; b) O. Kahn, C.-J. Martinez, *Science* **1998**, *279*, 44–48.
[4] a) *Topics in Current Chemistry Vols. 233–235: Spin Crossover in Transition Metal Compounds I–III* (Eds.: P. Gütlich, H. A. Goodwin), Springer-Verlag, Berlin, **2004**; b) J.-A. Real, A.-B. Gasper, M.-C. Muñoz, *Dalton Trans.* **2005**, 2062–2079.
[5] A. Bousseksou, G. Molnár, G. Matouzenko, *Eur. J. Inorg. Chem.* **2004**, 4353–4369.
[6] L.-A. Yatsunyk, F.-A. Walker, *Inorg. Chem.* **2004**, *43*, 757–777.
[7] a) G.-N. La Mar, F.-A. Walker in *The Porphyrins*, *Vol. IV* (Ed.: D. Dolphin), Academic Press, New York, **1979**, p. 61; b) S.-E. Creutz, J.-C. Peters, *Inorg. Chem.* **2016**, *55*, 3894–3906; c) H. Peltzold, P. Djomgoue, G. Hörner, J. M. Speck, T. Rüffer, D. Schaarschmidt, *Dalton Trans.* **2016**, *45*, 13798–13809; d) R. G. Miller, S. Brooker, *Inorg. Chem.* **2015**, *54*, 5398–5409.
[8] a) F. H. Köhler in *Magnetism: Molecules to Materials: Models and Experiments*, *Vol. IV* (Eds.: J.-S. Miller, M. Drillon), Wiley-VCH, Weinheim, **2001**, p. 379; b) F.-A. Walker in *The Porphyrin Handbook*, *Vol. 5* (Eds.: K.-M. Kadish, K.-M. Smith, R. Guilard), Academic Press, London, **2000**, p. 81.
[9] See, for example: S. Schlamp, K. Dankhoff, B. Weber, *New J. Chem.* **2014**, *38*, 1965.
[10] a) J. Mercurol, Y. Li, E. Pardo, O. Risset, M. Seuleiman, H. Roussèliere, R. Lecouëzec, M. Julve, *Chem. Commun.* **2010**, *46*, 8995–8997; b) A. Mondal, Y. Li, M. Seuleiman, M. Julve, L. Toupet, M. Buron-Le-Cointe, R. Lescouëzec, *J. Am. Chem. Soc.* **2013**, *135*, 1653–1656.
[11] a) A. Mondal, Y. Li, P. Herson, M. Seuleiman, M.-L. Boillot, E. Rivière, M. Julve, L. Rechignat, A. Bousseksou, R. Lescouëzec, *Chem. Commun.* **2012**, *48*, 5653–5655; b) A. Mondal, L.-M. Chamoreau, Y. Li, Y. Journaux, M. Seuleiman, R. Lescouëzec, *Chem. Eur. J.* **2013**, *19*, 7682–7685; c) A. Mondal, Y. Li, L.-M. Chamoreau, M. Seuleiman, L. Rechignat, A. Bousseksou, M.-L. Boillot, R. Lescouëzec, *Chem. Commun.* **2014**, *50*, 2893–2895.
[12] a) C. Graaf, C. Sousa, *Chem. Eur. J.* **2010**, *16*, 4550–4556; b) W. Gawelda, A. Cannizzo, V.-T. Pham, F. Mourik, C. Bressler, M. Chergui, *J. Am. Chem. Soc.* **2007**, *129*, 8199–8206; c) S. Dick, *Z. Kristallogr. New Cryst. Struct.* **1998**, *213*, 356.
[13] a) I.-G. Filippova, A. Simonov, M. Gdanets, V. Stavila, *J. Struct. Chem.* **2005**, *46*, 1095–1098; b) K. Teramoto, T. Kawasaki, T. Nishide, Y. Ikeda, *Acta Crystallogr., Sect. E: Struct. Rep. Online* **2015**, *71*, m8–m9; c) T. Ohshita, A. Tsukamoto, M. Senna, *Phys. Status Solidi A* **2004**, *201*, 762–768; d) Y. Umemura, Y. Minai, T. Tominaga, *J. Phys. Chem. B* **1999**, *103*, 647–652.
[14] a) P. Gütlich, A. Hauser, H. Spiering, *Angew. Chem. Int. Ed. Engl.* **1994**, *33*, 2024–2054; *Angew. Chem.* **1994**, *106*, 2109; b) P. Gütlich, A. Hauser, *Coord. Chem. Rev.* **1990**, *97*, 1–22; c) P. Guionneau, *Dalton Trans.* **2014**, *43*, 382–393.
[15] a) L. Bénisvy, J.-C. Chottard, J. Marrot, Y. Li, *Eur. J. Inorg. Chem.* **2005**, 999–1002; b) M.-P. Batten, A.-J. Canty, K.-J. Cavell, T. Rüther, B.-W. Skelton, A.-H. White, *Acta Crystallogr., Sect. C: Cryst. Struct. Commun.* **2004**, *60*, m316–m319; c) P.-C. Bruijnincx, I.-L. Buurmans, Y. Huang, G. Juhász, M. Viciano-Chumillas, M. Quesada, J. Reedijk, M. Lutz, A.-L. Spek, E. Münck, E.-L. Bominaar, R.-J. Klein Gebbink, *Inorg. Chem.* **2011**, *50*, 9243–9255.
[16] a) A. Scheja, D. Baabe, D. Menzel, C. Pietzonka, P. Schweyen, M. Bröring, *Chem. Eur. J.* **2015**, *21*, 14196–14204; b) J.-S. Pap, B. Kripli, M. Giorgi, J. Kaizer, G. Speier, *Trans. Met. Chem.* **2011**, *36*, 481–487; c) J.-S. Pap, V.

Bányai, D.-S. Szilvási, J. Kaizer, G. Speier, M. Giorgi, *Inorg. Chem. Commun.* **2011**, *14*, 1767–1772; d) J.-S. Pap, B. Kripli, V. Bányai, M. Giorgi, L. Korecz, T. Gajda, D. Arus, J. Kaizer, G. Speier, *Inorg. Chim. Acta* **2011**, *376*, 158–169.

[17] S. Alvarez, P. Alemany, D. Casanova, J. Cirera, M. Llunell, D. Avnir, *Coord. Chem. Rev.* **2005**, *249*, 1693–1708.

[18] a) D. Casanova, J. Cirera, M. Llunell, P. Alemany, D. Avnir, S. Alvarez, *J. Am. Chem. Soc.* **2004**, *126*, 1755–1763; b) J. Cirera, E. Ruiz, S. Alvarez, *Organometallics* **2005**, *24*, 1556–1562.

[19] a) R.-L. Jaffe, G.-D. Smith, *J. Chem. Phys.* **1996**, *105*, 2780–2788; b) C. Janiak, S. Temizdemir, S. Dechert, W. Deck, F. Girgsdies, J. Heinze, M.-J. Kolm, T.-G. Scharmann, O.-M. Zipffel, *Eur. J. Inorg. Chem.* **2000**, 1229–1241; c) V.-B. Medaković, M.-K. Milčić, G.-A. Bogdanović, S.-D. Zarić, *J. Inorg. Biochem.* **2004**, *98*, 1867–1873; d) J.-M. Sexton, A.-A. Elliott, A.-L. Steber, S.-A. Peebles, R.-A. Peebles, J.-L. Neill, M.-T. Muckle, B.-H. Pate, *Phys. Chem. Chem. Phys.* **2010**, *12*, 14263–14270.

[20] P. Hobza, H.-L. Selzle, E.-W. Schlag, *Chem. Rev.* **1994**, *94*, 1767–1785.

[21] a) N. N. L. Madhavi, G.-R. Desiraju, A.-K. Katz, H.-L. Carrell, A. Nangia, *Chem. Commun.* **1997**, 1953–1954; b) H.-C. Weiss, D. Blaser, R. Boese, B.-M. Doughan, M.-M. Haley, *Chem. Commun.* **1997**, 1703–1704; c) T. Steiner, M. Tamm, B. Lutz, J. van der Maas, *Chem. Commun.* **1996**, 1127–1128; d) P.-L. Anelli, P.-R. Ashton, R. Ballardini, V. Balzani, M. Delgado, M.-T. Gandolfi, T.-T. Goodnow, A.-E. Kaifer, D. Philip, *J. Am. Chem. Soc.* **1992**, *114*, 193.

[22] J. A. Réal, M.-C. Muñoz, E. Andrès, T. Granier, B. Gallois, *Inorg. Chem.* **1994**, *33*, 3587–3594.

[23] C.-P. Slichter, H.-G. Drickamer, *J. Chem. Phys.* **1972**, *56*, 2142–2160.

[24] J.-P. Tuchagues, A. Bousseksou, G. Molnár, J.-J. McGarvey, F. Varret in *Topics in Current Chemistry Vol. 235: Spin Crossover in Transition Metal Compounds* (Eds: P. Gütlich, H. A. Goodwin), Springer-Verlag, Berlin, **2004**, p. 85.

[25] G. Molnár, V. Niel, A.-B. Gaspar, J. A. Real, A. Zwick, A. Bousseksou, J.-J. McGarvey, *J. Phys. Chem. B* **2002**, *106*, 9701–9707.

[26] a) K.-S. Kumar, I. Salitros, B. Heinrich, O. Fuhr, M.-A. Ruben, *Mater. Chem.* **2015**, *3*, 11635–11644; b) T. Nakamoto, Z.-C. Tan, M. Sorai, *Inorg. Chem.* **2001**, *40*, 3805–3809.

[27] a) H.-S. Scott, T.-M. Ross, N.-F. Chilton, I.-A. Gass, B. Moubaraki, G. Chastanet, N. Paradis, J.-F. Létard, K.-R. Vignesh, G. Rajaraman, S.-R. Batten, K. Murray, *Dalton Trans.* **2013**, *42*, 16494–16509; b) V. Martínez, A.-B. Gaspar, M.-C. Muñoz, G.-V. Bukin, G. Levchenko, J. A. Real, *Chem. Eur. J.* **2009**, *15*, 10960–10971.

[28] H. Petzold, P. Djomgoue, G. Hörner, J.-M. Speck, T. Rüffer, D. Schaarschmidt, *Dalton Trans.* **2016**, *45*, 13798–13809.

[29] S. De, J.-R. Jiménez, Y. Li, L.-M. Chamoreau, A. Flambard, Y. Journaux, A. Bousseksou, R. Lescouëzec, *RSC Adv.* **2016**, *6*, 17456–17459.

[30] a) P. Roquette, A. Maronna, M. Reinmuth, E. Kaifer, M. Enders, H.-J. Himmel, *Inorg. Chem.* **2011**, *50*, 1942–1955; b) T.-E. Machonkin, W.-M. Westler, J.-L. Markley, *Inorg. Chem.* **2005**, *44*, 779–797; c) I. Bertini, C. Luccinat, *Coord. Chem. Rev.* **1996**, *150*, 77–110.

[31] J. Keeler, *Understanding NMR Spectroscopy*, *2nd ed.*, John Wiley & Sons, Ltd., Chichester, **2010**, p. 274.

[32] a) A. Donaire, J. Salgado, H.-R. Jimenez, J.-M. Moratal in *Nuclear Magnetic Resonance of Paramagnetic Molecules* (Ed.: G.-N. La Mar), Kluwer Academic Publishers, Dordrecht, **1995**, p. 213; b) Z. Wang, L. Que Jr. in *Nuclear Magnetic Resonance of Paramagnetic Molecules* (Ed.: G.-N. La Mar), Kluwer Academic Publishers, Dordrecht, **1995**, p. 193.

[33] C. Belle, C. Bougault, M.-T. Averbuch, A. Durif, J.-L. Pierre, J.-M. Latour, L. Le Pape, *J. Am. Chem. Soc.* **2001**, *123*, 8053–8066.

[34] R. J. Kurland, B. R. McGarvey, *J. Magn. Reson.* **1970**, *2*, 286–301.

[35] a) L. Banci, I. Bertini, C. Luchinat, R. Pierattelli, N.-V. Shokhirev, F.-A. Walker, *J. Am. Chem. Soc.* **1998**, *120*, 8472–8479; b) D.-L. Turner, *Eur. J. Biochem.* **1993**, *211*, 563–568.

[36] B. Weber, F.-A. Walker, *Inorg. Chem.* **2007**, *46*, 6794–6803.

[37] J.-P. Jesson in *Nuclear Magnetic Resonance of Paramagnetic Molecules* (Eds.: G.-N. La Mar, W.-D. Horrocks, R.-H. Holm), Academic Press, New York, **1973**.

[38] a) F.-M. Regueiro, B. Bensenane, E. Ruscsák, D. Esteban-Gómez, L.-J. Charbonnière, G. Tircsó, I. Tóth, A. de Blas, T. Rodríguez-Blas, C. Platas-Iglesias, *Inorg. Chem.* **2011**, *50*, 4125–4141; b) M. Purgel, Z. Baranyai, A. de Blas, T. Rodríguez-Blas, I. Bányai, C. Platas-Iglesias, I. Tóth, *Inorg. Chem.* **2010**, *49*, 4370–4382; c) D. J. Press, N. M. R. Mcneil, A. Rauk, T. G. Back, *J. Org. Chem.* **2012**, *77*, 9268–9276.

[39] The evaporation of the solvent above 350 K prevents the study at higher temperatures.

[40] W. Klaeui, W. Eberspach, P. Gütlich, *Inorg. Chem.* **1987**, *26*, 3977–3982.

[41] a) A. Flambard, F. H. Köhler, R. Lescouëzec, B. Revel, *Chem. Eur. J.* **2011**, *17*, 11567–11575; b) A. Flambard, F. H. Köhler, R. Lescouëzec, *Angew. Chem. Int. Ed.* **2009**, *48*, 1673–1676; *Angew. Chem.* **2009**, *121*, 1701.

[42] a) R.-K. Wilson, S. Brooker, *Dalton Trans.* **2013**, *42*, 12075–12078; b) S. Heider, H. Petzold, G. Teucher, *Eur. J. Inorg. Chem.* **2013**, 2382–2388.

[43] a) S.-K. Sur, *J. Magn. Reson.* **1989**, *82*, 169; b) D.-F. Evans, *J. Chem. Soc.* **1959**, 2003–2005.

[44] R.-C. Weast, M.-J. Astle, W.-H. Beyer in *Handbook of Chemistry and Physics*, *64th ed.*, CRC Press, Boca Raton, **1983**.

[45] G.-A. Bain, J.-F. Berry, *J. Chem. Educ.* **2008**, *85*, 532–536.

[46] See ref.[23]

[47] I. Bertini, P. Turano, A.-J. Vila, *Chem. Rev.* **1993**, *93*, 2833–2932.

[48] M. Reiher, O. Salomon, B. A. Hess, *Theor. Chem. Acc.* **2001**, *107*, 48–55.

[49] M. J. Swart, *J. Chem. Theory Comput.* **2008**, *4*, 2057.

[50] D. N. Bowman, E. Jakubikova, *Inorg. Chem.* **2012**, *51*, 6011–19.

[51] S. J. Grimme, *Comput. Chem.* **2006**, *27*, 1787–99.

[52] K. P. Kepp, *Coord. Chem. Rev.* **2013**, *257*, 196–209.

[53] G. R. Desiraju, T. Steiner, *The Weak Hydrogen Bond in Structural Chemistry and Biology*, Oxford University Press, Oxford, **1999**.

[54] J. Tomasi, B. Mennucci, R. Cammi, *Chem. Rev.* **2005**, *105*, 2999–3094.

[55] a) P. Lucas, N. El Mehdi, H.-A. Ho, D. Bélanger, L. Breau, *Synthesis* **2000**, *9*, 1253–1258; b) N. Braussaud, T. Ruther, J.-C. Kingsley, B.-W. Skelton, A.-H. White, *Synthesis* **2001**, *4*, 626–632.

[56] L. Peters, F.-M. Tepedino, T. Haas, W.-F. Heinemann, M. Wolf, N. Burzlaff, *Inorg. Chim. Acta* **2011**, *374*, 392–405.

[57] A. Altomare, G. Cascarano, C. Giacovazzo, A. Guagliardi, *J. Appl. Crystallogr.* **1993**, *26*, 343–350.

[58] G. M. Sheldrick, *Acta Crystallogr., Sect. A: Found. Crystallogr.* **2008**, *64*, 112–122.

[59] L. Palatinus, G. Chapuis, *J. Appl. Crystallogr.* **2007**, *40*, 786–790.

[60] L.-J. Farrugia, *J. Appl. Crystallogr.* **1999**, *32*, 837–838.

[61] P.-W. Betteridge, J.-R. Carruthers, R.-I. Cooper, K. Prout, D.-J. Watkin, *J. Appl. Crystallogr.* **2003**, *36*, 1487.

[62] F. Jensen in *Introduction to Computational Chemistry*, *2nd ed.*, John Wiley & Sons Ltd, Chichester, **2007**.

[63] M. J. Frisch, G. W. Trucks, H. B. Schlegel, G. E. Scuseria, M. A. Robb, J. R. Cheeseman, G. Scalmani, V. Barone, B. Mennucci, G. A. Petersson, H. Nakatsuji, M. Caricato, X. Li, H. P. Hratchian, A. F. Izmaylov, J. Bloino, G. Zheng, J. L. Sonnenberg, M. Hada, M. Ehara, K. Toyota, R. Fukuda, J. Hasegawa, M. Ishida, T. Nakajima, Y. Honda, O. Kitao, H. Nakai, T. Vreven, J. A. Montgomery Jr., J. E. Peralta, F. Ogliaro, M. Bearpark, J. J. Heyd, E. Brothers, K. N. Kudin, V. N. Staroverov, R. Kobayashi, J. Normand, K. Raghavachari, A. Rendell, J. C. Burant, S. S. Iyengar, J. Tomasi, M. Cossi, N. Rega, J. M. Millam, M. Klene, J. E. Knox, J. B. Cross, V. Bakken, C. Adamo, J. Jaramillo, R. Gomperts, R. E. Stratmann, O. Yazyev, A. J. Austin, R. Cammi, C. Pomelli, J. W. Ochterski, R. L. Martin, K. Morokuma, V. G. Zakrzewski, G. A. Voth, P. Salvador, J. J. Dannenberg, S. Dapprich, A. D. Daniels, Ö. Farkas, J. B. Foresman, J. V. Ortiz, J. Cioslowski, D. J. Fox, *Gaussian 09, Revision A.02*, Gaussian, Inc., Wallingford CT, **2016**.

[64] A.-D. Becke, *Phys. Rev. A* **1988**, *38*, 3098–3100.

[65] a) C. Lee, W. Yang, R.-G. Parr, *Phys. Rev. B* **1988**, *37*, 785–789; b) B. Miehlich, A. Savin, H. Stoll, H. Preuss, *Chem. Phys. Lett.* **1989**, *157*, 200–206.

[66] a) A. Schafer, H. Horn, R. Ahlrichs, *J. Chem. Phys.* **1992**, *97*, 2571–2577; b) A. Schafer, C. Huber, R. Ahlrichs, *J. Chem. Phys.* **1994**, *100*, 5829–5835.

[67] V.-A. Rassolov, J.-A. Pople, M.-A. Ratner, T.-L. Windus, *J. Chem. Phys.* **1998**, *109*, 1223–1229.

Received: August 24, 2017

 